HER◉N

Contents

MODELLING AND ANALYSIS OF RUBBERLIKE MATERIALS

R. de Borst
TNO Institute for Building Materials and Structures/
Delft University of Technology,
Dept. of Civil Engineering

P. A. J. van den Bogert
Delft University of Technology,
Dept. of Civil Engineering

J. Zeilmaker
Rijkswaterstaat
Formerly: TNO Plastics and Rubber Research Institute

Publication in HERON since 1970

Abstract

A numerical scheme for strictly and nearly incompressible rubberlike materials is described. A Total Lagrange description is adopted to describe the large deformations that occur. A separate interpolation for the displacements and the pressures is used to model the (near) incompressibility. The employed constitutive model can be classified as hyperelastic with the strain energy function being composed of a deviatoric and a volumetric contribution. Thus, the volumetric deformations can be controlled in a physically realistic manner, which is important since experimental evidence indicates that, although the ratio of bulk modulus over shear modulus is very large for rubbers, volumetric strains cannot be neglected. The second part of the paper is devoted to a number of practical examples. It is shown that finite elements are very useful for assessing the strength and deformation characteristics of rubber components, but that a number of questions that are important for practical structures, are still open.

MODELLING AND ANALYSIS OF RUBBERLIKE MATERIALS

1. Introduction

Rubbers and rubberlike materials are used less frequently in civil engineering practice than steel and concrete. Nevertheless, there is a growing need for an improved knowledge of and computational models for the mechanical behaviour of components composed of rubberlike materials, since such components are more and more used in critical parts of a structure. Examples are shock absorbers which prevent damage accumulation between steel and concrete parts of a structure, rubber parts which act as seals between parts of underwater tunnels and bearing platens of bridges. Failure of the rubber connection may lead to considerable damage.

Since the finite element method is widely employed in computational models for steel and concrete, it would be convenient if it could also be used for the analysis of rubber parts. Fortunately, it appears that the finite element method is also a powerful tool for the analysis of rubberlike solids. In fact, the first successful calculations date back to the late 1960s (see e.g., the book by Oden, [1]). Nevertheless, a number of problems which adhere to the application of the finite element method to *practical* problems concerning the analysis of rubber components still exist. These became apparent to the writers when they applied finite element techniques in conjunction with material models for rubber to some specific practical problems.

From the current experience of the writers, the problems with the application of the finite element method to rubber components relate to:

— properties of finite elements in relation to the incompressibility or near-incompressibility of most rubbers, and

— stability of the solution process, especially when thick components are considered in the compressive regime, and

— inadequacies of rubber models that are currently available in finite element codes.

The first problem arises from the fact that the incompressibility or near-incompressibility imposes constraints on the degrees-of-freedom of the elements. This phenomenon, known as 'locking', causes an overstiff solution. In recent years, much research effort has been devoted to this problem and, at least in two-dimensional applications, finite elements have been developed which no longer suffer from this behaviour. For three-dimensional applications the solution is more complicated.

The biggest problem is probably the second issue, namely the stability of the numerical process. It is known that stability and uniqueness of solution are guaranteed only

below a threshold level of loading in finite elasticity [2,3]. Nonetheless, convergence difficulties are not mentioned in most numerical examples reported in the literature. This is probably because the majority of the examples concerns the behaviour of rubber components in tension. Then, the writers did not have problems with convergence either. For components that were subjected to compressive loading, an inability to converge was often found long before the design load had been applied, the precise point of divergence somewhat depending on the shape factor of the specimen. Slender specimens could be analysed further than stubby specimens.

The third problem is the discrepancy between some elementary rubber models and the real physical behaviour. Almost all numerical codes incorporate an incompressible rubber model. The writers found that this assumption is too great a simplification of reality. Depending on the amount of soot, industrial rubbers are usually much more compressible than an assumption of incompressibility suggests. Of course, rubbers are still incompressible in a mechanical sense since the ratio of bulk modulus to shear modulus (in the ground state) is very large.

In this article, we will attempt to contribute to bridging the gap between theoretical finite element analyses of imaginary rubber parts and the often rather crude design procedures of rubber components. Therefore, an important part of this article is devoted to numerical analyses of some practical structures. Where possible, analyses will be compared with experiments. Discrepancies will be pointed out and the improvements that are needed will be discussed.

In the spirit that theoretical developments and practical applications should proceed at approximately equal pace, some attention is also given to the determination of material parameters for the models from laboratory tests. To give a complete picture, the discussions of the parameter determination and the applications will be preceded by a treatment of the material models and the finite element techniques that have been used.

2. Constitutive equations

In this chapter an overview will be given of the material models that have been used in the examples. New models are not presented in this chapter. It is rather included for sake of completeness and in order to introduce the stress and strain measures that have been used in the analysis and in the determination of the parameters of the material models. Readers who are not familiar with mathematical models for the mechanical behaviour of rubberlike materials are urged to read this chapter, since knowledge thereof is needed not only for the finite element formulation to be discussed in the next chapter, but also for the determination of the material parameters.
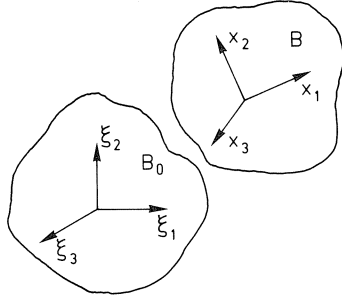
Fig. 2.1. Current and reference configuration.

2.1 Kinematic preliminaries

Let us consider a body B with coordinates (ξ_1, ξ_2, ξ_3) in the undeformed configuration B_0 and coordinates (x_1, x_2, x_3) in the current configuration (Figure 2.1). We can define a function $\mathbf{x}(\xi)$ that maps the undeformed configuration onto the deformed configuration, as follows:

$$\mathbf{x}(\xi): \quad \xi \rightarrow \mathbf{x}. \tag{2.1}$$

In eq. (2.1) the vector $\mathbf{x}$ that points to a material point in the deformed configuration is a function of the vector ξ that defines a material point in the undeformed state. The coordinates of $\mathbf{x}$ are called Eulerian or spatial coordinates, while those of ξ are termed Lagrange or material coordinates. A small, elementary volume that is contained somewhere in the body will in general undergo a *translation,* a *rotation* and a *deformation.* For constitutive relations, which basically set a relation between the stress and the deformation, the rigid body motions (rotation and translation) must be eliminated from the total movement of an elementary volume. For elimination of the rigid translation, we consider the matrix $\mathbf{F}$ that arises when the spatial coordinates are differentiated with respect to the material coordinates:

$$\mathbf{F} = \mathbf{x}\nabla_\xi. \tag{2.2}$$

The symbol ∇_ξ is the gradient operator which carries out differentiation with respect to the material coordinates (ξ_1, ξ_2, ξ_3). The operator ∇ is applied from the right, i.e.

$$\mathbf{F} = \begin{bmatrix} x_1 \\ x_2 \\ x_3 \end{bmatrix} \begin{bmatrix} \dfrac{\partial}{\partial \xi_1} & \dfrac{\partial}{\partial \xi_2} & \dfrac{\partial}{\partial \xi_3} \end{bmatrix} = \begin{bmatrix} \dfrac{\partial x_1}{\partial \xi_1} & \dfrac{\partial x_1}{\partial \xi_2} & \dfrac{\partial x_1}{\partial \xi_3} \\[2mm] \dfrac{\partial x_2}{\partial \xi_1} & \dfrac{\partial x_2}{\partial \xi_2} & \dfrac{\partial x_2}{\partial \xi_3} \\[2mm] \dfrac{\partial x_3}{\partial \xi_1} & \dfrac{\partial x_3}{\partial \xi_2} & \dfrac{\partial x_3}{\partial \xi_3} \end{bmatrix},$$

so that $\mathbf{F}^T = \nabla_\xi \mathbf{x}$. Next consider an additional translation $\mathbf{c}$ that is added to the vector $\mathbf{x}$, such that $\mathbf{x}' = \mathbf{x} + \mathbf{c}$. Since $\mathbf{c}$ is not a function of ξ, differentiation with respect to ξ yields

$$\mathbf{F} = \mathbf{x}' \nabla_\xi.$$

Obviously, the deformation gradient $\mathbf{F}$ describes the deformation and the rotation of a body for each material point, but the amount of translation is not contained in this matrix.

To also remove the rotation, we decompose $\mathbf{F}$ in a multiplicative sense:

$$\mathbf{F} = \mathbf{R}\,\mathbf{U}. \tag{2.3}$$

Without proof (see e.g., [4]), it is now asserted that the matrix $\mathbf{R}$ contains pure rotations and the matrix $\mathbf{U}$ contains pure deformations. The multiplicative decomposition of eq. (2.3) is called the *polar decomposition* and separates the rigid rotations from the pure deformations. It is noted that only for the case of small deformations, the multiplicative decomposition can be replaced by an additive decomposition.

Unfortunately, the strain measure $\mathbf{U}$ is not easy to compute. Rather, $\mathbf{U}^2$ is computed. By virtue of the fact that $\mathbf{R}$ is an orthogonal matrix, we have the identity $\mathbf{R}^T = \mathbf{R}^{-1}$. Consequently, $\mathbf{R}^T\mathbf{R} = \mathbf{I}$, $\mathbf{I}$ being the unit matrix, and premultiplication of eq. (2.3) by the transpose of the deformation gradient, $\mathbf{F}^T$, results in

$$\mathbf{C} = \mathbf{U}^2 = \mathbf{F}^T\mathbf{F}, \tag{2.4}$$

and the quantity $\mathbf{C}$ also measures the pure deformation. In the literature (e.g., [4]) it is referred to as 'right stretch tensor' or 'right Cauchy-Green tensor'. As we will show in the sequel, $\mathbf{C}$ reduces to the unit matrix for the undeformed state. This means that in the undeformed state we have a deformation of "1" which is not very appealing to engineers who are accustomed to strain measures that are zero in the undeformed state. Therefore, the Green-Lagrange strain tensor $\boldsymbol{\gamma}$ is also used frequently to characterise large deformations. It is obtained by subtracting the unit matrix $\mathbf{I}$ from the right stretch tensor $\mathbf{C}$ and

6

dividing the result by a factor 2:

$$\boldsymbol{\gamma} = \frac{1}{2}(\mathbf{C} - \mathbf{I}).$$
(2.5)

In the chapter on determination of the material properties use will frequently be made of the so-called principal stretches λ_1, λ_2 and λ_3. These quantities are the ratios of the new and the old lengths of an elementary cube, referred to the principal axes of the stretch tensor $\mathbf{C}$. In this coordinate system the deformation gradient $\mathbf{F}$ is given by:

$$\mathbf{F} = \begin{bmatrix} \lambda_1 & 0 & 0 \\ 0 & \lambda_2 & 0 \\ 0 & 0 & \lambda_3 \end{bmatrix}.$$

With aid of (2.4) we can then derive that the normal stretches are given by $C_{11} = \lambda_1^2$ etc. while all shear stretches vanish. In the undeformed configuration the principal stretches equal unity and C_{11}, C_{22} and C_{33} are therefore also equal to 1 in the undeformed state. The normal components $\gamma_{11}, \gamma_{22}, \gamma_{33}$ of the strain tensor $\boldsymbol{\gamma}$ on the other hand are given by $\gamma_{11} = \frac{1}{2}(\lambda_1^2 - 1)$ etc., so that γ_{11}, γ_{22} and γ_{33} vanish in the undeformed state.

2.2 Strain energy function

The most notable mechanical properties of rubbers are their ability to undergo extremely large deformations, up to several hundred percent, without tearing and the fact that the strains are almost instantaneously recoverable. For these reasons, rubbers are often termed 'ideally elastic' materials. An ideally elastic material is defined by a unique relation between stress and strain, the stress being dependent only on the current stress or strain state and not on the deformation history as is the case for many other engineering materials. Properties like a unique relation between stress and strain and no energy dissipation in a closed cycle of application and removal of stress, can be ensured by requiring the strain energy density e to be a function of the strain tensor $\boldsymbol{\gamma}$ only. In consideration of eqs. (2.4) and (2.5) we can alternatively require e to be a single-valued function of the right stretch tensor $\mathbf{C}$: $e = e(\mathbf{C})$. In a purely mechanical theory, i.e. without consideration of thermal effects, an equilibrium state is characterised by the vanishing of the first variation of the difference of the total deformation energy E of the body and the potential energy U of the loads:

$$\delta(E - U) = 0.$$
(2.6)

In the current configuration E is given by

7

$$E = \int_V \rho \, e \, (\mathbf{C}) \mathrm{d}V \qquad (2.7)$$

with ρ the mass density in the actual state. When $\mathbf{g}$ is the gravity acceleration vector and when a traction $\mathbf{t}$ acts on an elementary surface $\mathrm{d}S$ with a normal vector $\mathbf{n}$ in the current configuration, U is given by

$$U = \int_V \rho \mathbf{x}^{\mathrm{T}} \mathbf{g} \mathrm{d}V + \int_S \mathbf{x}^{\mathrm{T}} \mathbf{t} \mathrm{d}S. \qquad (2.8)$$

Since e is a function of the right stretch tensor only, the variation of the strain energy density e is given by

$$\delta e = 2 \, \mathrm{tr} \left[\delta \mathbf{F} \frac{\partial e}{\partial \mathbf{C}} \mathbf{F}^{\mathrm{T}} \right], \qquad (2.9)$$

where tr denotes the trace of a matrix. Combining (2.6)-(2.9) and assuming that the load is conservative, we obtain

$$\int_V 2\rho \, \mathrm{tr} \left[\delta \mathbf{F} \frac{\partial e}{\partial \mathbf{C}} \mathbf{F}^{\mathrm{T}} \right] \mathrm{d}V - \int_V \rho \delta \mathbf{x}^{\mathrm{T}} \mathbf{g} \mathrm{d}V - \int_S \delta \mathbf{x}^{\mathrm{T}} \mathbf{t} \mathrm{d}S = 0. \qquad (2.10)$$

Invoking the divergence theorem for the first integral,

$$\int_V 2\rho \, \mathrm{tr} \left[\delta \mathbf{F} \frac{\partial e}{\partial \mathbf{C}} \mathbf{F}^{\mathrm{T}} \right] \mathrm{d}V = \int_S 2\rho \delta \mathbf{x}^{\mathrm{T}} \mathbf{F} \frac{\partial e}{\partial \mathbf{C}} \mathbf{F}^{\mathrm{T}} \mathbf{n} \, \mathrm{d}S - \int_V \delta \mathbf{x}^{\mathrm{T}} \mathrm{div} \left[2\rho \mathbf{F} \frac{\partial e}{\partial \mathbf{C}} \mathbf{F}^{\mathrm{T}} \right] \mathrm{d}V,$$

with div denoting the divergence operator, this equation can be rewritten as

$$\int_S \delta \mathbf{x}^{\mathrm{T}} \left[2\rho \mathbf{F} \frac{\partial e}{\partial \mathbf{C}} \mathbf{F}^{\mathrm{T}} \mathbf{n} - \mathbf{t} \right] \mathrm{d}S - \int_V \delta \mathbf{x}^{\mathrm{T}} \left[\mathrm{div}(2\rho \mathbf{F} \frac{\partial e}{\partial \mathbf{C}} \mathbf{F}^{\mathrm{T}}) + \rho \mathbf{g} \right] \mathrm{d}V = 0, \qquad (2.11)$$

whence

$$\mathrm{div} \left[2\rho \mathbf{F} \frac{\partial e}{\partial \mathbf{C}} \mathbf{F}^{\mathrm{T}} \right] + \rho \mathbf{g} = \mathbf{0}, \qquad (2.12)$$

for each material point within the body, and

$$t = 2\rho F \frac{\partial e}{\partial C} F^T n \qquad (2.13)$$

on the surface S of the body in the current state. Introducing the Cauchy stress tensor

$$\tau = 2\rho F \frac{\partial e}{\partial C} F^T \qquad (2.14)$$

eqs. (2.12) and (2.13) can be rewritten as

$$\text{div}\tau + \rho g = 0, \qquad (2.15)$$

and

$$t = \tau n. \qquad (2.16)$$

It is seen from eq. (2.16) that the Cauchy stress tensor τ sets the relation between the traction t and the normal vector n on a surface S in the current state. It is emphasised that (2.15) and (2.16) have been derived in the actual configuration. Consequently, the Cauchy stress τ is also a function of the current coordinates and differentiation is carried out with respect to x.

Although knowledge of the Cauchy stresses is often necessary to assess whether the actual stresses that occur in rubber components can be accepted, their use in numerical codes is not convenient, since the expression (2.14) for τ involves the deformation gradient F, which is still unknown. For computational purposes it is therefore convenient to introduce the second Piola-Kirchhoff stress tensor σ,

$$\sigma = 2 \frac{\partial W}{\partial C} \qquad (2.17)$$

with $W = \rho_0 e$ the strain energy function, and ρ_0 the mass density in the reference state. In view of eq. (2.14) the relation between the physically relevant Cauchy stress τ and the auxiliary stress measure σ reads:

$$\tau = \frac{\rho}{\rho_0} F \sigma F^T.$$

Because of conservation of mass of an elementary volume dV,

$$\rho_0 dV_0 = \rho dV$$

and since

$$\frac{dV}{dV_0} = \lambda_1 \lambda_2 \lambda_3 = \det \mathbf{F}$$

the relation between $\boldsymbol{\tau}$ and $\boldsymbol{\sigma}$ is also written as

$$\boldsymbol{\tau} = (\det \mathbf{F})^{-1} \mathbf{F} \boldsymbol{\sigma} \mathbf{F}^{\mathrm{T}}. \tag{2.18}$$

An important simplification is obtained when the material is isotropic throughout the loading process. Then, the strain energy function W is only a function of the three stretch invariants

$$I_1 = C_{11} + C_{22} + C_{33}, \tag{2.19}$$

$$I_2 = C_{11}C_{22} + C_{22}C_{33} + C_{33}C_{11} - C_{12}C_{21} - C_{23}C_{32} - C_{31}C_{13}, \tag{2.20}$$

$$I_3 = C_{11}C_{22}C_{33} + 2C_{12}C_{23}C_{31} - C_{11}C_{23}C_{32} - C_{22}C_{31}C_{13} - C_{33}C_{12}C_{21} \tag{2.21}$$

of the right stretch tensor $\mathbf{C}$:

$$W = W(I_1, I_2, I_3),$$

where $W(3,3,1) = 0$ must hold as W must vanish in the undeformed state. With definition (2.17) for the second Piola-Kirchhoff pseudo-stress tensor $\boldsymbol{\sigma}$, we get

$$\boldsymbol{\sigma} = 2 \left[\frac{\partial W}{\partial I_1} \frac{\partial I_1}{\partial \mathbf{C}} + \frac{\partial W}{\partial I_2} \frac{\partial I_2}{\partial \mathbf{C}} + \frac{\partial W}{\partial I_3} \frac{\partial I_3}{\partial \mathbf{C}} \right]. \tag{2.22}$$

The gradients $\partial I_1/\partial \mathbf{C}$, $\partial I_2/\partial \mathbf{C}$ and $\partial I_3/\partial \mathbf{C}$ are elaborated in the Appendix.

The task of constructing a function W that accurately captures experimental data, is alleviated considerably if it is assumed that the strain energy is separable into a volumetric part that is purely dependent on the volumetric deformations, and a deviatoric part that is a function of the distortion. The volumetric strain is entirely characterised by the third invariant I_3 of the right-stretch tensor $\mathbf{C}$. In the principal directions the expression for I_3 reduces to $I_3 = C_{11}C_{22}C_{33}$, or using the principal stretches $\lambda_1, \lambda_2, \lambda_3$:

$$I_3 = (\lambda_1 \lambda_2 \lambda_3)^2.$$

Since, for an elementary volume, $\lambda_1 \lambda_2 \lambda_3 = dV/dV_0$, I_3 sets a relation between the volume in the deformed configuration dV and the volume in the undeformed

configuration dV_0:

$$I_3 = \left(\frac{dV}{dV_0} \right)^2 .$$

As a first step in writing W as the sum of a volumetric and a deviatoric part, we will decompose W into $W^*(I_1, I_2)$ and $f(I_3)$:

$$W = W^*(I_1, I_2) + f(I_3) \tag{2.23}$$

such that $W^*(3,3) = 0$ and $f(1) = 0$. A problem for the identification of $f(I_3)$ is that W^* is also affected by purely volumetric deformations. This problem may be solved by introducing the modified set of stretch invariants J_1, J_2 and J_3:

$$J_1 = I_1 I_3^{-1/3}, \tag{2.24}$$

$$J_2 = I_2 I_3^{-2/3}, \tag{2.25}$$

$$J_3 = I_3^{1/2}, \tag{2.26}$$

which transformation has first been used by Penn [5] and has later also been used in [6,7]. With aid of the modified invariants, eq. (2.23) is rewritten as

$$W = W^*(J_1, J_2) + f(J_3 - 1), \tag{2.27}$$

which formulation provides a complete separation of the distortional and the volumetric work. It is noted that by making f a function of $J_3 - 1$, the condition that f vanishes in the undeformed state is automatically ensured. When using expression (2.27) as the strain energy function of a slightly compressible solid rather than eq. (2.23), the Piola-Kirchhoff stresses are given by:

$$\sigma = 2 \left[\frac{\partial W^*}{\partial J_1} \frac{\partial J_1}{\partial \mathbf{C}} + \frac{\partial W^*}{\partial J_2} \frac{\partial J_2}{\partial \mathbf{C}} + f'(J_3 - 1) \frac{\partial J_3}{\partial \mathbf{C}} \right], \tag{2.28}$$

where f' denotes differentiation with respect to J_3.

The change of invariants implies that, in principle, the material constants that are used when W^* is expressed in I_1 and I_2, must be modified. Yet, the compressibility of rubbers is usually very small, the deviation of J_3 from unity being mostly less than 10^{-4} [8], and an insignificant error is committed when the original constants are used in

connection with the modified invariants.

A simple form for f, which as we will see in the next chapter is also convenient for implementation in numerical codes, is obtained by starting from a linear relationship between the hydrostatic pressure p and the volume change ΔV:

$$-p = \kappa \frac{\Delta V}{V_0}. \qquad (2.29)$$

with κ the bulk modulus. Experimental evidence [5,6] suggests that κ is independent of J_3 for a wide range of pressures, but also seems to suggest that κ is a function of J_1 and J_2. When introducing such a dependence, the separability of (2.23) is lost and, therefore, κ will be assumed to be a material constant in this study. From the preceding definitions, it is found that

$$\frac{\Delta V}{V_0} = \frac{V}{V_0} - 1 = J_3 - 1,$$

so that (2.29) is rewritten as

$$-p = \kappa(J_3 - 1). \qquad (2.30)$$

Basically, the hydrostatic pressure is defined as minus one-third of the trace of the *Cauchy* stress tensor τ:

$$-p = \frac{1}{3} \operatorname{tr}(\tau) \qquad (2.31)$$

For purely volumetric deformations, all principal stretches are equal to λ, so that the deformation gradient $\mathbf{F}$ is given by

$$\mathbf{F} = \lambda \mathbf{I},$$

with $\mathbf{I}$ the unit matrix. Accordingly, relation (2.18) between the Cauchy and the second Piola-Kirchhoff stress tensor simplifies to

$$\tau = \lambda^{-1} \sigma,$$

and the hydrostatic pressure is given by

$$-p = \frac{1}{3} \lambda^{-1} \operatorname{tr}(\sigma)$$

Furthermore, the contribution of the deviatoric part W^* of the strain energy vanishes under an all-round uniform pressure p, so that in view of (2.28), the Piola-Kirchhoff

stress tensor is given by

$$\sigma = 2f'(J_3 - 1)\frac{\partial J_3}{\partial \mathbf{C}}.$$

Using the definitions given in the Appendix, the following expression for the hydrostatic pressure p ensues for purely volumetric deformations:

$$-p = f'(J_3 - 1). \tag{2.32}$$

Equating expressions (2.30) and (2.32) results in the following differential equation

$$\kappa(J_3 - 1) = f'(J_3 - 1).$$

Considering that f must vanish for $J_3 = 1$, this differential equation can be solved to yield

$$f(J_3 - 1) = \frac{1}{2}\kappa(J_3 - 1)^2. \tag{2.33}$$

Substitution of (2.33) in eq. (2.27) results in the strain energy function:

$$W = W^*(J_1, J_2) + \frac{1}{2}\kappa(J_3 - 1)^2. \tag{2.34}$$

A further simplification occurs if the bulk modulus κ is set equal to infinity. Then $J_3 = 1$ (or alternatively $I_3 = 1$) so that $J_3 - 1$ vanishes. Since $(J_3 - 1)^2$ approaches zero faster than κ tends to infinity, the second term in (2.34) vanishes, and the strain energy function reduces to

$$W = W^*(J_1, J_2), \tag{2.35}$$

or, since $I_1 = J_1, I_2 = J_2$ for $I_3 = 1$,

$$W = W^*(I_1, I_2). \tag{2.36}$$

Most currently published finite element calculations [8-11] assume the incompressible formulation (2.36) to model rubber behaviour. Yet, the assumption of incompressibility, which is nearly always made in numerical analyses of rubber components, is too crude for many industrial rubbers. This is shown in Figure 2.2, which shows the dependence of the bulk modulus in the ground state (= the undeformed state) as a function of the amount of soot. A significant variation of the compressibility with the percentage of soot in the rubber is observed. Consequently, finite element analyses that á priori assume incompressibility will not always give a realistic prediction of the stresses and especially
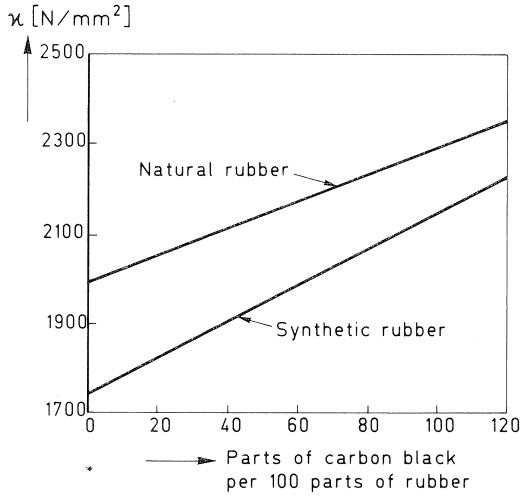
Fig. 2.2. The bulk modulus in the ground state as a function of
the amount of soot for industrial rubbers.

the deformations of rubber components.

2.3 Mooney-Rivlin material representation

The simplest choice for W^* is a linear function of I_1 and I_2:

$$W^* = K_1(I_1 - 3) + K_2(I_2 - 3), \tag{2.37}$$

in which the constants -3 have been introduced to achieve that W^* be zero in a strain-free state. Approximation (2.37) for the strain energy function of an incompressible rubber has first been hypothesised by Mooney [12] and has later been generalised by Rivlin [13] to include higher order terms. Relation (2.37) is known as the Mooney-Rivlin model for incompressible rubbers.

Although the Mooney-Rivlin model has originally been proposed for strictly incompressible rubbers, it can of course also be used to model the distortional response of a compressible rubber. For this purpose (2.37) is replaced by

$$W^* = K_1(J_1 - 3) + K_2(J_2 - 3). \tag{2.38}$$

Strictly speaking, the constants K_1 and K_2 must be modified when replacing (2.37) by (2.38), but the fact that the deviation of J_3 from 1 hardly ever exceeds 10^{-4} warrants the assumption that the same K_1 and K_2 can be used in (2.37) and (2.38) for all practical

14

purposes.

To gain some insight in the physical meaning of the material constants K_1 and K_2, we will consider the instantaneous stiffness in the undeformed state. To this end, we first substitute (2.38) in (2.34)

$$W = K_1(J_1-3)+K_2(J_2-3)+\frac{1}{2}\kappa(J_3-1)^2, \tag{2.39}$$

so that the second Piola-Kirchhoff stresses are given by

$$\sigma = 2\left[K_1\frac{\partial J_1}{\partial \mathbf{C}}+K_2\frac{\partial J_2}{\partial \mathbf{C}}+\kappa(J_3-1)\frac{\partial J_3}{\partial \mathbf{C}}\right]. \tag{2.40}$$

Next, we consider a state of pure shear. For such a deformation $J_3=1$, so that (2.40) reduces to

$$\sigma = 2\left[K_1\frac{\partial J_1}{\partial \mathbf{C}}+K_2\frac{\partial J_2}{\partial \mathbf{C}}\right],$$

or using (2.24), (2.25) and the fact that pure shear is an isochoric deformation ($J_3=1$),

$$\sigma = 2\left[K_1\frac{\partial I_1}{\partial \mathbf{C}}+K_2\frac{\partial I_2}{\partial \mathbf{C}}-\frac{1}{3}(K_1I_1+2K_2I_2)\frac{\partial I_3}{\partial \mathbf{C}}\right]. \tag{2.41}$$

Differentiating this expression so as to obtain an incremental relation that defines the tangential stiffness, it is found that

$$\dot{\sigma} = 2\left[K_2\frac{\partial^2 I_2}{\partial \mathbf{C}^2}-\frac{1}{3}(K_1I_1+2K_2I_2)\frac{\partial^2 I_3}{\partial \mathbf{C}^2}-\frac{1}{3}(K_1\frac{\partial I_1}{\partial \mathbf{C}}+2K_2\frac{\partial I_2}{\partial \mathbf{C}})\frac{\partial I_3}{\partial \mathbf{C}}\right]\dot{\mathbf{C}}.$$

With aid of the expressions for $\partial I_1/\partial \mathbf{C}$ etc. as given in the Appendix we can derive for the shear stress, say σ_{12}, in the ground state ($I_1=I_2=3$), that

$$\dot{\sigma}_{12} = 2(K_1+K_2)\dot{C}_{12}. \tag{2.42}$$

In the undeformed state, $\dot{\sigma}_{12}$ can be conceived as the true stress rate and $\dot{C}_{12}$ can be replaced by the engineering shear strain rate $\dot{\gamma}_{12}$. Consequently, $2(K_1+K_2)$ has the meaning of a shear modulus, say μ, when the strains become small.

3. Finite element implementation

In this chapter the governing finite element equations will be derived. An approach is adopted in which different degrees of interpolation are used for the displacement and the pressure field. The chapter is intended for readers who have been exposed to numerical treatments before. Readers who are primarily interested in the modelling of rubber components with aid of finite elements may omit this chapter and may directly proceed to the chapter on the determination of material constants.

3.1 Equilibrium equations

As a point of departure for the derivation of the governing finite element equations, we shall take eq. (2.10), albeit in a slightly modified form:

$$\int_V 2\rho \, \mathrm{tr}\left[\frac{\partial e}{\partial \mathbf{C}} \mathbf{F}^\mathrm{T} \delta \mathbf{F} \right] \mathrm{d}V - \int_V \rho \delta \mathbf{x}^\mathrm{T} \mathbf{g} \mathrm{d}V - \int_S \delta \mathbf{x}^\mathrm{T} \mathbf{t} \mathrm{d}S = 0.$$

For deformation problems in solid mechanics, this form of the equilibrium equation is not convenient as it takes the current, hitherto unknown configuration as reference configuration. For rubber elasticity, where there exists a physically meaningful relation with the undeformed configuration throughout the entire loading process, the latter configuration is better suited to this purpose. For transformation of the equilibrium condition to the undeformed configuration we use conservation of mass for an elementary volume $\mathrm{d}V$

$$\rho_0 \mathrm{d}V_0 = \rho \mathrm{d}V,$$

and we observe that, for conservative loading, the force on an elementary surface $\mathrm{d}S$ remains constant,

$$\mathbf{t}_0 \mathrm{d}S_0 = \mathbf{t} \mathrm{d}S,$$

with $\mathbf{t}_0$ the traction referred to the surface of the undeformed body $\mathrm{d}S_0$ (nominal traction). With aid of these identities, the equilibrium equation can be restated as

$$\int_{V_0} 2\rho_0 \, \mathrm{tr}\left[\frac{\partial e}{\partial \mathbf{C}} \mathbf{F}^\mathrm{T} \delta \mathbf{F} \right] \mathrm{d}V_0 - \int_{V_0} \rho_0 \delta \mathbf{x}^\mathrm{T} \mathbf{g} \mathrm{d}V_0 - \int_{S_0} \delta \mathbf{x}^\mathrm{T} \mathbf{t}_0 \mathrm{d}S_0 = 0. \tag{3.1}$$

Recalling the definition of the second Piola-Kirchhoff stress tensor (eq. (2.17))

$$\sigma = 2\rho_0 \frac{\partial e}{\partial \mathbf{C}},$$

we obtain instead of (3.1)

$$\int_{V_0} \mathrm{tr}\left[\sigma \mathbf{F}^{\mathrm{T}}\delta\mathbf{F}\right] dV_0 - \int_{V_0} \rho_0 \delta\mathbf{x}^{\mathrm{T}}\mathbf{g}dV_0 - \int_{S_0} \delta\mathbf{x}^{\mathrm{T}}\mathbf{t}_0 dS_0 = 0.$$

In consideration of the definition of γ (eqs. (2.4) and (2.5)), the variation of γ reads

$$\delta\gamma = \frac{1}{2}\left[\mathbf{F}^{\mathrm{T}}\delta\mathbf{F} + \delta\mathbf{F}^{\mathrm{T}}\mathbf{F}\right] \tag{3.2}$$

so that, by virtue of the symmetry of the stress tensor σ, the equilibrium equation is now written as

$$\int_{V_0} \mathrm{tr}\left[\sigma\delta\gamma\right] dV_0 - \int_{V_0} \rho_0 \delta\mathbf{x}^{\mathrm{T}}\mathbf{g}dV_0 - \int_{S_0} \delta\mathbf{x}^{\mathrm{T}}\mathbf{t}_0 dS_0 = 0. \tag{3.3}$$

Nonlinear calculations must be carried out in a number of small loading steps so as to ensure stability of the iterative procedure that is employed to solve the resulting set of nonlinear algebraic equations. To this end we rewrite (3.3) as follows

$$\int_{V_0} \mathrm{tr}\left[(\sigma^t + \Delta\sigma)\delta\gamma\right] dV_0 + \int_{V_0} \rho_0 \delta\mathbf{x}^{\mathrm{T}}\mathbf{g}dV_0 - \int_{S_0} \delta\mathbf{x}^{\mathrm{T}}\mathbf{t}_0 dS_0 = 0, \tag{3.4}$$

with $\Delta\sigma$ the increment of the Piola-Kirchhoff stress tensor and σ^t its value at time t. It is now important to recall that, although all quantities are referred to the undeformed configuration, the virtual work equation has been set up at $t' = t + \Delta t$. This implies that the variation $\delta\gamma$ also has to be evaluated for $t' = t + \Delta t$ and consequently, the spatial coordinates (x_1, x_2, x_3) that enter eq. (3.4) are coordinates at $t' = t + \Delta t$. Operating on the position vector $\mathbf{x}$ in the deformed configuration in a similar fashion as on the stresses,

$$\mathbf{x}^{t+\Delta t} = \mathbf{x}^t + \Delta\mathbf{x},$$

so that, in view of (2.2), (3.2) effectively reads

$$\delta\gamma^{t+\Delta t} = \frac{1}{2}\Big[(\nabla_\xi x^t)(\delta x \nabla_\xi) + (\nabla_\xi \delta x)(x^t \nabla_\xi)$$

$$+ (\nabla_\xi \Delta x)(\delta x \nabla_\xi) + (\nabla_\xi \delta x)(\Delta x \nabla_\xi) \Big], \tag{3.5}$$

we can rewrite $\delta\gamma^{t+\Delta t}$ as

$$\delta\gamma^{t+\Delta t} = \delta\varepsilon + \delta\eta. \tag{3.6}$$

The contribution $\delta\varepsilon$,

$$\delta\varepsilon = \frac{1}{2}\Big[(\nabla_\xi x^t)(\delta x \nabla_\xi) + (\nabla_\xi \delta x)(x^t \nabla_\xi) \Big], \tag{3.7}$$

is not a function of the increments Δx, while $\delta\eta$ is linear in Δx:

$$\delta\eta = \frac{1}{2}\Big[(\nabla_\xi \Delta x)(\delta x \nabla_\xi) + (\nabla_\xi \delta x)(\Delta x \nabla_\xi) \Big]. \tag{3.8}$$

Substitution of (3.6) in (3.4) and rearranging we obtain

$$\int\limits_{V_0} \mathrm{tr}\Big[\Delta\sigma\delta\varepsilon \Big] dV_0 + \int\limits_{V_0} \mathrm{tr}\Big[\sigma^t \delta\eta \Big] dV_0 + \int\limits_{V_0} \mathrm{tr}\Big[\Delta\sigma\delta\eta \Big] dV_0 =$$

$$\int\limits_{V_0} \delta x^T \rho_0 g \, dV_0 + \int\limits_{S_0} \delta x^T t_0 \, dS_0 - \int\limits_{V_0} \delta\varepsilon^T \sigma^t \, dV_0.$$

In the sequel of this chapter, we will usually write the stress and strain tensors σ and γ as a vectors instead of as matrices. Then, the preceding equation changes into

$$\int\limits_{V_0} \delta\varepsilon^T \Delta\sigma \, dV_0 + \int\limits_{V_0} \delta\eta^T \sigma^t \, dV_0 + \int\limits_{V_0} \delta\eta^T \Delta\sigma \, dV_0 =$$

$$\int\limits_{V_0} \rho_0 \delta x^T g \, dV_0 + \int\limits_{S_0} \delta x^T t_0 \, dS_0 - \int\limits_{V_0} \delta\varepsilon^T \sigma^t \, dV_0. \tag{3.9}$$

In principle, the incremental constitutive relation for hyperelastic materials can be derived by differentiation of eq. (2.22). Finite elements, however, tend to 'lock', not only in strictly, but in practice also in nearly incompressible media [7,16]. This 'locking' phenomenon causes an overstiff solution. Predictions for (nearly) incompressible solids may be improved by using a separate interpolation for displacements and pressures. Then, it is more convenient to commence from (2.28) rather than from (2.22):

18

$$\sigma = 2 \left[\frac{\partial W^*}{\partial J_1} \frac{\partial J_1}{\partial \mathbf{C}} + \frac{\partial W^*}{\partial J_2} \frac{\partial J_2}{\partial \mathbf{C}} + f'(J_3 - 1) \frac{\partial J_3}{\partial \mathbf{C}} \right].$$

Since a separate interpolation of the displacement and the pressure field is desired, $f'(J_3 - 1)$ is replaced by $-p$ in accordance with eq. (2.32):

$$\sigma = 2 \left[\frac{\partial W^*}{\partial J_1} \frac{\partial J_1}{\partial \mathbf{C}} + \frac{\partial W^*}{\partial J_2} \frac{\partial J_2}{\partial \mathbf{C}} - p \frac{\partial J_3}{\partial \mathbf{C}} \right]. \tag{3.10}$$

By differentiation of (3.10) we obtain the relation between the stress increment $\Delta\sigma$, the increment $\Delta\gamma$ of the Green-Lagrange strain tensor and the pressure increment Δp :

$$\Delta\sigma = \mathbf{D}\Delta\gamma - 2\Delta p \frac{\partial J_3}{\partial \mathbf{C}} \tag{3.11}$$

where the matrix $\mathbf{D}$ contains the instantaneous stiffness moduli,

$$\mathbf{D} = 4 \left[\frac{\partial^2 W^*}{\partial J_1^2} \frac{\partial J_1}{\partial \mathbf{C}} \frac{\partial J_1}{\partial \mathbf{C}} + \frac{\partial^2 W^*}{\partial J_1 \partial J_2} \frac{\partial J_1}{\partial \mathbf{C}} \frac{\partial J_2}{\partial \mathbf{C}} + \frac{\partial W^*}{\partial J_1} \frac{\partial^2 J_1}{\partial \mathbf{C}^2} + \right.$$

$$\left. \frac{\partial^2 W^*}{\partial J_2 \partial J_1} \frac{\partial J_2}{\partial \mathbf{C}} \frac{\partial J_1}{\partial \mathbf{C}} + \frac{\partial^2 W^*}{\partial J_2^2} \frac{\partial J_2}{\partial \mathbf{C}} \frac{\partial J_2}{\partial \mathbf{C}} + \frac{\partial W^*}{\partial J_2} \frac{\partial^2 J_2}{\partial \mathbf{C}^2} - p \frac{\partial^2 J_3}{\partial \mathbf{C}^2} \right]. \tag{3.12}$$

Inserting (3.11) in (3.9) we obtain

$$\int_{V_0} \delta\varepsilon^{\mathrm{T}} \mathbf{D}\Delta\varepsilon \, dV_0 + \int_{V_0} \delta\eta^{\mathrm{T}} \sigma^t \, dV_0 - \int_{V_0} 2\delta\varepsilon^{\mathrm{T}} \frac{\partial J_3}{\partial \mathbf{C}} \Delta p \, dV_0 =$$

$$\int_{V_0} \rho_0 \delta\mathbf{x}^{\mathrm{T}} \mathbf{g} \, dV_0 + \int_{S_0} \delta\mathbf{x}^{\mathrm{T}} \mathbf{t}_0 \, dS_0 - \int_{V_0} \delta\varepsilon^{\mathrm{T}} \sigma^t \, dV_0. \tag{3.13}$$

In (3.13) the contributions $\int \delta\varepsilon^{\mathrm{T}} \mathbf{D}\Delta\eta \, dV_0$ and $\int \delta\eta^{\mathrm{T}} \mathbf{D}\Delta\gamma \, dV_0$ which are nonlinear in $\Delta\mathbf{x}$ have been omitted. This has no impact on the accuracy of the results provided that the stresses are obtained from the current strain state with a proper relation (e.g., (2.22) or (2.28)). It simply serves the purpose of obtaining a properly linearized tangent stiffness on the left hand side of the equation.

19

For the spatial discretization it is assumed that the continuum is divided in an arbitrary number of finite elements. Let the continuous displacement field $\mathbf{u}$ be interpolated by polynomials h_1, h_2 etc. Assembling the interpolation polynomials in a matrix $\mathbf{H}$ and the nodal displacements in a vector $\mathbf{a}$, we can formally write (e.g., [15-18])

$$\mathbf{u} = \mathbf{Ha}. \tag{3.14}$$

Furthermore, the relation between the part of the strain increment $\Delta\boldsymbol{\varepsilon}$ that is linear in the displacement increment and $\Delta\mathbf{u}$ (note that $\Delta\mathbf{u} = \Delta\mathbf{x}$) reads

$$\Delta\boldsymbol{\varepsilon} = \mathbf{L}\Delta\mathbf{u},$$

with $\mathbf{L}$ a matrix that contains differential operators and is derived from eq. (3.7). The relation between the linear part of the strain increment $\Delta\boldsymbol{\varepsilon}$ and the incremental nodal displacements is then given by

$$\Delta\boldsymbol{\varepsilon} = \mathbf{B}_L \Delta\mathbf{a} \tag{3.15}$$

and similarly

$$\delta\boldsymbol{\varepsilon} = \mathbf{B}_L \delta\mathbf{a}$$

with $\mathbf{B}_L = \mathbf{LH}$. Explicit forms of $\mathbf{B}_L$ matrices are given in [18,19] for various configurations. Using eq. (3.15) the first contribution to the tangent stiffness can be rewritten as

$$\int_{V_0} \delta\boldsymbol{\varepsilon}^\mathrm{T} \mathbf{D} \Delta\boldsymbol{\varepsilon}\, dV_0 = \delta\mathbf{a}^\mathrm{T} \left[\int_{V_0} \mathbf{B}_L^\mathrm{T} \mathbf{D} \mathbf{B}_L \, dV_0 \right] \Delta\mathbf{a}$$

In a similar fashion the second contribution to the tangent stiffness can be rewritten as

$$\int_{V_0} \delta\boldsymbol{\eta}^\mathrm{T} \boldsymbol{\sigma}^t \, dV_0 = \delta\mathbf{a}^\mathrm{T} \left[\int_{V_0} \mathbf{B}_{NL}^\mathrm{T} \boldsymbol{\Sigma} \mathbf{B}_{NL} \, dV_0 \right] \Delta\mathbf{a}$$

where $\boldsymbol{\Sigma}$ is a matrix representation of the second Piola-Kirchhoff stress tensor and $\mathbf{B}_{NL}$ again contains differential operators [18,19].

The pressure p that enters eq. (3.13) is an additional unknown. It is usually interpolated by a polynomial of a lower degree than the displacements (e.g., [7,16,18]). Assembling the interpolation polynomials for the pressure in a matrix $\mathbf{N}$, we have

20

$$\mathbf{p} = \mathbf{N}p, \tag{3.16}$$

with p the continuous pressure distribution and $\mathbf{p}$ the values of the nodal pressure. Note that the nodes at which the pressure is an unknown need not coincide with the nodes at which the displacements are variables. With the interpolation of (3.16) the third term on the left hand side is written as

$$\int_{V_0} 2\delta\boldsymbol{\varepsilon}^{\mathrm{T}} \frac{\partial J_3}{\partial \mathbf{C}} \Delta p \, dV_0 = \delta\mathbf{a}^{\mathrm{T}} \int_{V_0} 2\mathbf{B}_L^{\mathrm{T}} \frac{\partial J_3}{\partial \mathbf{C}} \mathbf{N} dV_0 \Delta\mathbf{p}$$

Noting that $\delta\mathbf{x}^t = 0$, so that $\delta\mathbf{x} = \delta\mathbf{u}$, inserting (3.14)-(3.16) in (3.13), and considering that the result must hold for any virtual displacement $\delta\mathbf{a}$, the following set of nonlinear algebraic equations is obtained

$$\left[\int_{V_0} \mathbf{B}_L^{\mathrm{T}} \mathbf{D} \mathbf{B}_L \, dV_0 + \int_{V_0} \mathbf{B}_{NL}^{\mathrm{T}} \boldsymbol{\Sigma} \mathbf{B}_{NL} \, dV_0 \right] \Delta\mathbf{a} - \left[\int_{V_0} 2\mathbf{B}_L^{\mathrm{T}} \frac{\partial J_3}{\partial \mathbf{C}} \mathbf{N} dV_0 \right] \Delta\mathbf{p} =$$

$$\int_{V_0} \rho_0 \mathbf{H}^{\mathrm{T}} \mathbf{g} dV_0 + \int_{S_0} \mathbf{H}^{\mathrm{T}} \mathbf{t}_0 dS_0 - \int_{V_0} \mathbf{B}_L^{\mathrm{T}} \boldsymbol{\sigma}^t dV_0. \tag{3.17}$$

3.2 Weak formulation of the volumetric stress-strain relation

Equation (3.17) generates $2n$ equations, n being the number of displacement nodes, but has $2n + m$ degrees-of-freedom, m being the number of pressure nodes. The missing m equations can be constructed by virtue of the volumetric stress-strain relation (2.30):

$$\kappa(J_3^{t+\Delta t} - 1) + p^{t+\Delta t} = 0.$$

The weak form of this equation is given by

$$\int_{V_0} [(J_3^{t+\Delta t} - 1) + e p^{t+\Delta t}] \delta p dV_0 = 0, \tag{3.18}$$

with $e = \kappa^{-1}$ the compressibility. Decomposing in known values at $t' = t$ and increments yields

$$-\int_{V_0} [\Delta J_3 + e\,\Delta p\,]\delta p\,\mathrm{d}V_0 = \int_{V_0} [(J_3^t - 1) + ep^t\,]\delta p\,\mathrm{d}V_0.$$

Since

$$\Delta J_3 = 2\left(\frac{\partial J_3}{\partial \mathbf{C}}\right)^{\mathrm{T}} \Delta\boldsymbol{\gamma}$$

eq. (3.18) can be restated as

$$-\int_{V_0} 2\delta p\left(\frac{\partial J_3}{\partial \mathbf{C}}\right)^{\mathrm{T}} \Delta\boldsymbol{\gamma}\,\mathrm{d}V_0 - e\int_{V_0} \Delta p\,\delta p\,\mathrm{d}V_0 = \int_{V_0} [(J_3^t - 1) + ep^t\,]\delta p\,\mathrm{d}V_0,$$

so that, employing (3.15) and (3.16), linearizing in the sense that $\Delta\boldsymbol{\varepsilon}$ is substituted for $\Delta\boldsymbol{\gamma}$ and noting that the resulting expression must hold for any virtual pressure δp, we obtain

$$-\int_{V_0} 2\mathbf{N}^{\mathrm{T}}\left(\frac{\partial J_3}{\partial \mathbf{C}}\right)^{\mathrm{T}} \mathbf{B}_L\,\mathrm{d}V_0\,\Delta\mathbf{a} - e\int_{V_0} \mathbf{N}\mathbf{N}^{\mathrm{T}}\mathrm{d}V_0\,\Delta\mathbf{p} = \int_{V_0} [(J_3^t - 1) + ep^t\,]\mathbf{N}^{\mathrm{T}}\mathrm{d}V_0. \quad (3.19)$$

The sets of equations (3.17) and (3.19) generate as much equations as unknowns.

Next, the unbalanced force vector $\mathbf{F}_a$,

$$\mathbf{F}_a = \int_{V_0} \rho_0 \mathbf{H}^{\mathrm{T}}\mathbf{g}\mathrm{d}V_0 + \int_{S_0} \mathbf{H}^{\mathrm{T}}\mathbf{t}_0 \mathrm{d}S_0 - \int_{V_0} \mathbf{B}_L^{\mathrm{T}}\boldsymbol{\sigma}^t\,\mathrm{d}V_0, \qquad (3.20)$$

the vector $\mathbf{F}_b$,

$$\mathbf{F}_b = \int_{V_0} [(J_3^t - 1) + ep^t\,]\mathbf{N}^{\mathrm{T}}\mathrm{d}V_0, \qquad (3.21)$$

and the auxiliary matrices

$$\mathbf{K}_a = \int_{V_0} \mathbf{B}_L^{\mathrm{T}}\mathbf{D}\mathbf{B}_L\,\mathrm{d}V_0 + \int_{V_0} \mathbf{B}_{NL}^{\mathrm{T}}\boldsymbol{\Sigma}\mathbf{B}_{NL}\,\mathrm{d}V_0, \qquad (3.22)$$

$$\mathbf{K}_p = -\int_{V_0} 2\mathbf{B}_L^{\mathrm{T}}\frac{\partial J_3}{\partial \mathbf{C}}\mathbf{N}\mathrm{d}V_0, \qquad (3.23)$$

and $\mathbf{M}$,

22

$$M = -\int_{V_0} NN^T dV_0,$$ (3.24)

are introduced. With the definitions (3.20)-(3.24), eqs. (3.17) and (3.19) can be formulated in a compact manner:

$$\begin{bmatrix} K_a & K_p \\ K_p^T & e M \end{bmatrix} \begin{bmatrix} \Delta a \\ \Delta p \end{bmatrix} = \begin{bmatrix} F_a \\ F_b \end{bmatrix}.$$ (3.25)

A simplification can be achieved when the pressure degrees of freedom are eliminated at element level by a static condensation process [16,18]. When applying such a process in an incremental-iterative procedure, some care must be exercised with regard to the moments that compression of the element stiffness matrix and expansion for the internal degrees of freedom take place. To demonstrate this, we will describe the local compression/expansion process of a static condensation procedure in somewhat greater detail. To this end, we first express the pressure degrees of freedom in terms of the displacements:

$$\Delta p = \kappa M^{-1}[F_b - K_p^T \Delta a],$$ (3.26)

where it is recalled that $\kappa = e^{-1}$. Inserting (3.26) in the first equation of (3.25) yields:

$$[K_a - \kappa K_p M^{-1} K_p^T] \Delta a = F_a - \kappa K_p M^{-1} F_b.$$ (3.27)

The stiffness matrix and the right hand side vector at global level are derived from eq. (3.27). After solving for the incremental displacements Δa, the pressure increments Δp at element level are computed from eq. (3.26). It is of utmost importance that the expansion of (3.26) is done with the *same* matrices K_p and M as that have been used in the compression of (3.27). This is particularly so when a full Newton-Raphson method is employed, since the vector F_b may considerably deviate from zero during the equilibrium iterations. The danger of using an erroneous right hand side transpires when it is considered that the force vectors F_a and F_b are usually set up at the *end* of an iteration. The force vector $F_a - \kappa K_p M^{-1} F_b$ that is to be used *in the next iteration* must be computed with the tangential submatrix K_p which is, however, not available *until the beginning of the next iteration*. Consequently, the right hand side vector for the new iteration cannot be set up at the end of the old iteration, but can only be calculated after the tangential stiffness matrices have been set up at the beginning of the new iteration. If $F_a - \kappa K_p M^{-1} F_b$ is computed with the current, old matrix K_p, the quadratic convergence of Newton's method is lost.

o   Displacement nodes
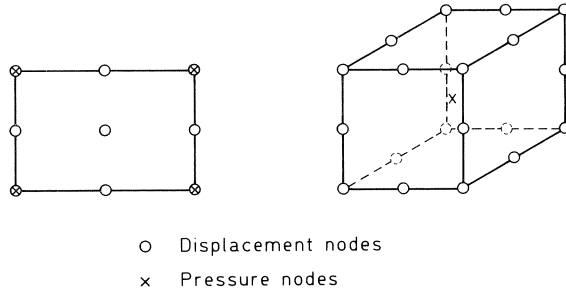
x   Pressure nodes

Fig. 3.1. Elements with separate interpolation for displacements and
pressures as have been used in this study.

From the preceding discussion it also transpires that the pressures become discontinuous
at the element interfaces. Effectively, this means that there is no longer a need to define
the degrees of freedom of the pressures at the element interfaces [7,16]. Nevertheless, the
pressure degrees of freedom have been chosen to be in the corners of the element for the
plane strain and the axisymmetric elements that have been used in this study. To be pre-
cise, a quadrilateral element with nine nodes for the displacement degrees of freedom,
and four nodes for the pressure degrees of freedom has been used. For the three-
dimensional analyses, an twenty-noded element with a constant pressure distribution has
been employed (see Figure 3.1), although it is recognised that superior elements have
recently been developed for three-dimensional analyses [20].

It is finally noted that strict incompressibility can be enforced by letting the bulk
modulus κ go to infinity, or alternatively, by setting $e = 0$. The set of equations (3.25)
then reduces to

$$
\begin{bmatrix} \mathbf{K}_a & \mathbf{K}_p \\ \mathbf{K}_p^{\mathrm{T}} & \mathbf{0} \end{bmatrix} \begin{bmatrix} \Delta \mathbf{a} \\ \Delta \mathbf{p} \end{bmatrix} = \begin{bmatrix} \mathbf{F}_a \\ \mathbf{F}_b \end{bmatrix},
\tag{3.28}
$$

where $\mathbf{F}_b$ is now given by:

$$
\mathbf{F}_b = \int_{V_0} (J_3^t - 1) \mathbf{N}^{\mathrm{T}} \mathrm{d}V_0.
$$

Unfortunately, the structure of (3.28) is unsuitable for most currently available linear
equation solvers because of the presence of zero entries on the main diagonal of the com-
posite matrix. This problem can be circumvented by relaxing the strict incompressibility

condition and assigning e a small value, e.g., 10^{-6}-10^{-8}. It then becomes unimportant which function f is selected for the volumetric part of the stored energy function as long as it is a convex function that satisfies $f(1)=0$ and $f \neq 0$ otherwise. For instance, the function

$$f = \frac{1}{2}\ln(J_3^2)$$

has been used in some of the examples where the strictly incompressible Mooney-Rivlin model has been adopted (see also [8-10]).

4. Determination of the material constants

In equation (2.37) the strain energy function for the Mooney-Rivlin material representation has been given. It is the purpose of this Chapter to show how the material constants K_1 and K_2 which appear in (2.37) can be determined from a simple uniaxial elongation test. In principle, the treatment will be given for a strictly incompressible material. For a nearly compressible rubber the same constants K_1 and K_2 are used, which implies that in this case the computed values for K_1 and K_2 are only approximations, albeit very good approximations, since the influence of the compressibility on the values of K_1 and K_2 is negligible.

For the particular case of simple axial elongation, we set the ratio of the new length over the original length equal to λ (compare the definition of the principal stretches in Chapter 2). For an incompressible material the volume remains unchanged, so that the principal stretch ratios λ_1, λ_2 and λ_3 are given by:

$$\lambda_1 = \lambda \qquad \lambda_2 = \lambda_3 = \lambda^{-1/2}. \tag{4.1}$$

Inserting (4.1) in expression (2.41) for the second Piola-Kirchhoff stress we obtain for an incompressible Mooney-Rivlin model:

$$\sigma_{11} = 2[K_1 + 2K_2\lambda^{-1} - \frac{1}{3}(K_1 I_1 + 2K_2 I_2)\lambda^{-2}] \tag{4.2}$$

for the axial principal stress and

$$\sigma_{22} = 2[K_1 + K_2(\lambda^2 + \lambda^{-1}) - \frac{1}{3}(K_1 I_1 + 2K_2 I_2)\lambda] \tag{4.3}$$

for either of the transverse principal stresses. In uniaxial tension, σ_{22} must vanish, whence
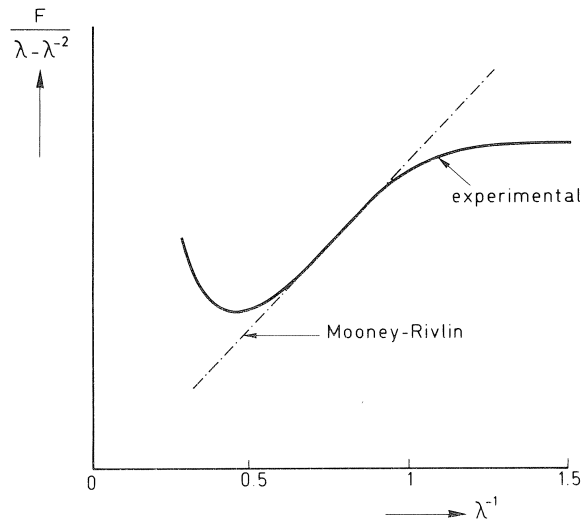
Fig. 4.1. Calibration of the Mooney-Rivlin constants K_1 and K_2.

$$\frac{1}{3}(K_1 I_1 + 2K_2 I_2) = \lambda^{-1}[K_1 + K_2(\lambda^2 + \lambda^{-1})].$$

Substitution of this expression in (4.2) yields

$$\sigma_{11} = 2\lambda^{-2}(\lambda^2 - \lambda^{-1})[K_1 + \lambda^{-1}K_2]. \tag{4.4}$$

According to eq. (2.18) the relation between the Cauchy stress, which gives the force per unit deformed cross section, and the second Piola-Kirchhoff stress is given by

$$\tau_{11} = \lambda^2 \sigma_{11},$$

so that

$$\tau_{11} = 2(\lambda^2 - \lambda^{-1})[K_1 + \lambda^{-1}K_2]. \tag{4.5}$$

The corresponding force F per unit unstrained cross-section becomes:

$$F = \tau_{11}\lambda^{-1} = 2(\lambda - \lambda^{-2})[K_1 + \lambda^{-1}K_2],$$

or, dividing by $2(\lambda - \lambda^{-2})$,

26

$$\frac{F}{2(\lambda - \lambda^{-2})} = K_1 + \lambda^{-1} K_2 . \qquad (4.6)$$

Fig. 4.1 presents a typical result for a rubber specimen undergoing a uniaxial deformation. In this figure, $\frac{1}{2} F / (\lambda - \lambda^{-2})$ is plotted as a function of λ^{-1}. It is observed that the Mooney-Rivlin model (the dash-dotted line in Figure 4.1) is only able to describe the material behaviour reasonably for values of λ^{-1} that range from 0.90 to 0.45, but that for other values of λ^{-1} deviations occur between theory and experiment.

According to (4.6) the slope of the Mooney-Rivlin approximation determines the constant K_2. Having estimated K_2, the second constant, K_1, can be determined by inserting an arbitrary pair of F and λ in eq. (4.6).

The actual execution of the elongation test requires some care. In the examples to be discussed in the next chapters, the following procedure has been followed. First, the sample is heated to the test temperature (23, 40, 65, 75°C) for 15 minutes. Then, tension-bars, either model C according to the ASTM D412 code, or samples with a length of 100 mm. and a width of 10 mm., are prestressed five times up to an extension ratio of 2 with a deformation rate of 100 mm/min. A Zwick drawbench type 1445 has been used for this purpose. The Mooney-Rivlin parameters K_1 and K_2 are calculated from a subsequent test up to an extension ratio of 1.90 with a drawbench speed of 1 mm/min. The prestressing is necessary because there is a considerable decrease in K_2 during this treatment. The amount of decrease of K_2 depends on the kind of filler that is used. Table 4.1 lists the influence of various kinds of filler on K_1 and K_2 for S.B.R. rubber.

Table 4.1. Influence of filler on decrease in K_1, K_2-values for a S.B.R. rubber [21].

Filler	first cycle		second cycle	
	$K_1 [N/mm^2]$	$K_2 [N/mm^2]$	$K_1 [N/mm^2]$	$K_2 [N/mm^2]$
SAF	0.26	1.04	0.23	0.43
HAF-LS	0.20	0.64	0.18	0.34
HAF-HS	0.24	0.84	0.24	0.37
GPF	0.22	0.64	0.19	0.48
SRF	0.26	0.58	0.15	0.39
No filler	0.13	0.17	0.12	0.16

HAF = High Abrasion Furnace   SAF = Super Abrasion Furnace
LS = Low Structure   GPF = General Purpose Furnace
HS = High structure   SRF = Semi Reinforced Furnace

5. Suspension ring

This chapter deals with the first of the three examples that are reported in this study. It is emphasised that all three examples relate to experience from practical applications. In this respect the present study differs from most other studies that are reported in the literature, since the examples contained therein are usually of a more academic nature. The example discussed in this chapter is a suspension ring which is prestressed by an internal gas pressure. Since this type of loading primarily induces tensile stresses in the suspension ring, stability problems are not encountered, although the deformations become quite large.

5.1 Description of the problem

The suspension ring is an important feature of the visco-seal that has been developed by Neratoom BV (Figure 5.1). The purpose of the seal is to prohibit transportation of gas from room A to room B. Due to small out-of-balance vibrations of the driving-shaft some displacement in the seal will remain, which, without precautions, will damage the visco-seal. The function of the suspension ring is to reduce the displacements of the rotating inner bush of the visco-seal.

The high demands made upon the suspension ring necessitate an investigation of the stress distribution and the displacements of a number of designs under operating conditions. From practical experience it is known that the rubber-steel bonding and internal tearing of the rubber product often cause trouble. A proper assessment of the different geometries requires that special attention be paid to the reliability of the rubber-steel interface. The danger of separation of the rubber from the steel driving-shaft can be reduced by enforcing a homogeneous shear stress distribution and avoiding tensile stress concentrations near the rubber-steel interface and the free surface with the gas room.

5.2 Design conditions

For the analysis of the mechanical behaviour of the suspension ring the design conditions as listed in Table 5.1 are of interest. With regard to these data the following remarks are made. The quoted temperature range is used to determine the values of the material properties. In other words: the stress-strain relation is influenced by the temperature in the sense that the constants K_1 and K_2 of the Mooney-Rivlin strain energy function are dependent on the temperature (see §2.3 for the description of the model and Ch. 4 for the determination of the constants). Thermal expansion and shrinkage have not been taken into account in the calculations. The centrifugal forces as introduced by the rotation of the visco-seal, are, compared with the internal gas pressure of 5.6 bar, very small and are therefore neglected. Consequently, only load related to the internal gas pressure is applied in the computations.
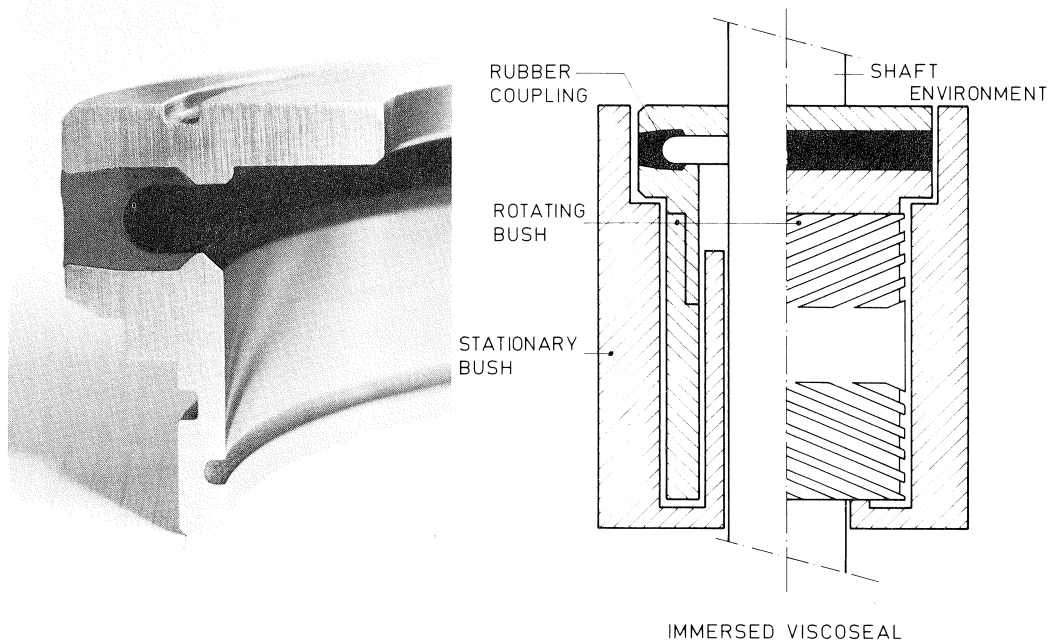
RUBBER
COUPLING

SHAFT

ENVIRONMENT

ROTATING
BUSH

STATIONARY
BUSH

IMMERSED VISCOSEAL

Fig. 5.1. Construction detail of the suspension ring.

Table 5.1. Design conditions of suspension ring.

Temperature range:	20 - 100°C
Internal gas pressure:	5.6 bar (room B)
External gas pressure:	0.0 bar (room A)
Speed of revolution:	50 - 960 r.p.m.
Lateral stiffness:	less than 600 N/mm
Overall axial load:	less than 1000 N
	(depending on the inner diameter
	of the suspension ring).

5.3 Results

In this study four geometrically different models have been analysed as to come to an optimal design of the rubber product from a engineering point of view. The first model, which is shown in Figure 5.2 together with the other designs, is the primary or original
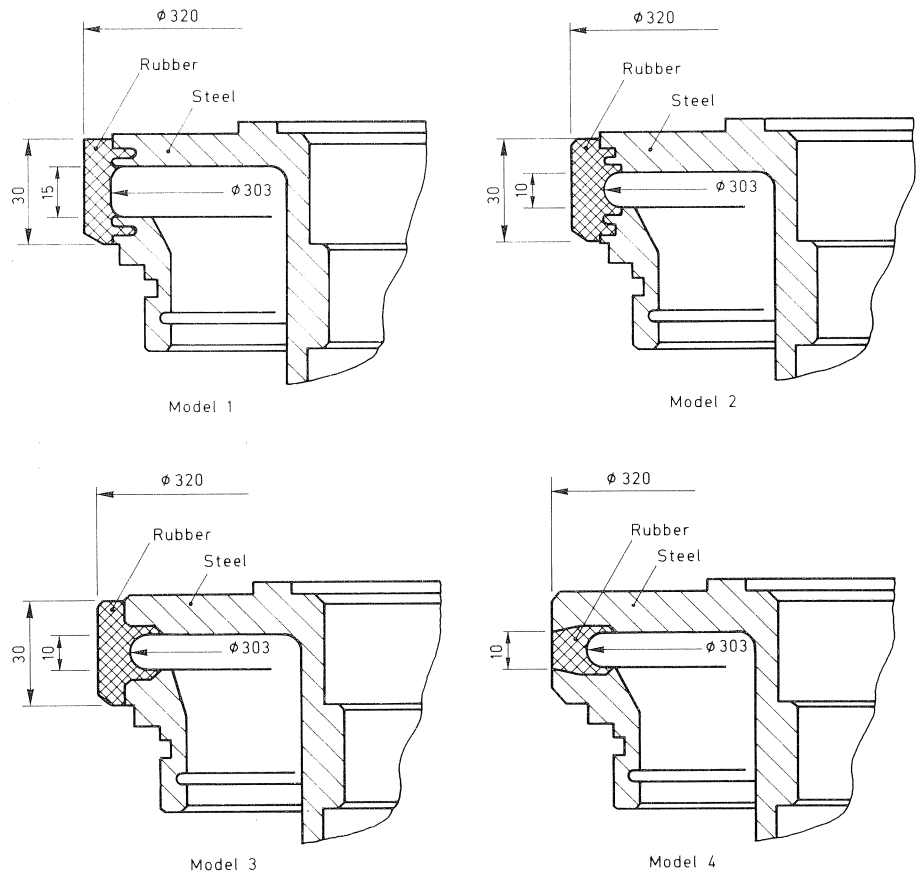
Fig. 5.2. Analysed designs of the suspension ring.

design of the suspension ring, while the models two, three and four are successive improvements. The models are loaded by a uniformly distributed pressure along the boundary CDF, and a vertical, downwardly directed, concentrated force in point G (see Figure 5.3 for the location of these points). The two steel parts of the visco-seal, which are connected by the rubber suspension ring, can only undergo a relative vertical displacement. This is accomplished by supporting both degrees-of-freedom of the nodes of the element meshes along the border CAB, tying the vertical degrees-of-freedom of the nodes along the boundaries FGH to the vertical displacement of point G and by supporting the horizontal degrees-of-freedom along FGH. For some of the designs the separation of the rubber from the steel is simulated by releasing some supported or tyed degrees-of-freedom near the points C and F. An incompressible Mooney-Rivlin stored energy function has been utilised with the constants $K_1 = 0.227 \, \text{N/mm}^2$ and $K_2 = 0.376 \, \text{N/mm}^2$.

30
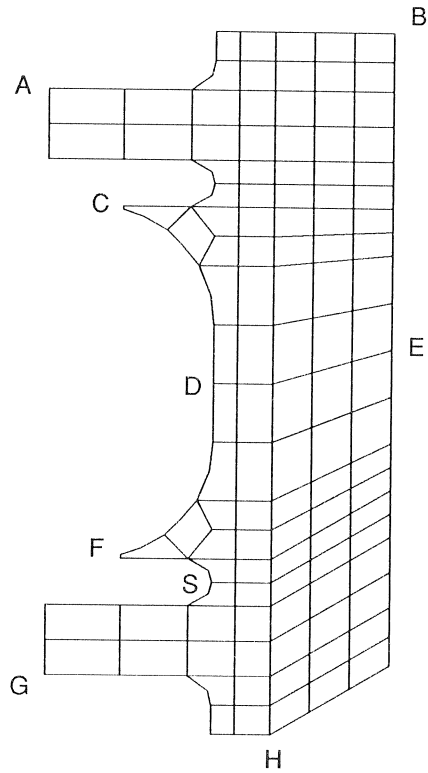
Fig. 5.3. Element mesh and significant points for model 1.

The four designs have been modelled with plane strain elements as well as with axisymmetric elements. As already noted in Ch. 3, nine-noded elements with a bilinear pressure distribution have been used. Most of the plane strain calculations have been carried out with the reduced 2*2 integration scheme. At higher loading levels such a rule can result in spurious kinematic modes. An example is shown in Figure 5.4. To reduce the possibility that spurious modes occur, a 3*3 integration scheme can be used. Even for such an integration rule, the possibility that such modes are found can not be eliminated completely (see e.g., [22,23]), but the chances are reduced significantly when compared to 2*2 point Gaussian integration. A drawback of using a 'full' 3*3 integration rule is that the solution may become overstiff. In particular, as already alluded to in Ch. 3, there exists the possibility of 'locking' for incompressible or nearly incompressible materials [7,16,24]. A comparison for some of the calculations showed, however, that the displacements of a model with a 2*2 integration rule hardly exceeded those of the same model but calculated with a 3*3 integration rule (Table 5.3). Another disadvantage of 3*3 point integration is the fact that the stresses may be less accurate than for 2*2 integrated
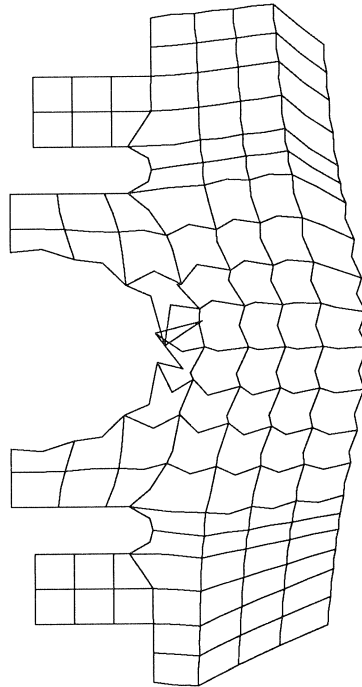
Fig. 5.4. Spurious kinematic mode encountered in an analysis for model 1.

elements. Table 5.4 shows that in the case considered this effect must have been of minor importance, since the stresses are of the same order.

5.3.1 Model 1

For the first geometry, the original design, the following calculations have been carried out:

A. Calculation of the axial displacement due to a known axial force.

B. Calculation of the displacement and stresses due to a internal gas pressure of 5.6 bar at a temperature of 65°C.

C. Calculation of the displacements and stresses due to the internal gas pressure of 5.6 bar at a temperature of 65°C, but with a simulation of the separation of the rubber-steel interface.

— Results under A: First the result are briefly presented for the case of a concentrated axial force. This calculation has been carried out to verify the theory and the applied material constants determined on a laboratory sheet. The results have been summarised in Table 5.2, and show that there is a good agreement between theory and practice. This outcome gives confidence in the results of the other calculations.

Table 5.2. Displacements u_z at point G for load case A.

load [N]	calculated [mm]	measured [mm]
1250	1.4	1.6
2500	3.0	3.1

— Results under B: In Figure 5.5 the deformed mesh and the distribution of the Cauchy stresses are given for the first geometry at a load level of 5.6 bar, which load level is defined to coincide with a load factor of 1.0. Figure 5.5 shows that the true (Cauchy) stresses unfortunately reach a maximum at places where, due to the manufacturing process, it is difficult to obtain a good bonding between rubber and steel (near point S). The critical bonding places are loaded in tension, while, from a engineering point of view, it is preferable that bonding surfaces are subjected to compressive or shear stresses. From Figure 5.5 it also appears that the stresses in the rubber elements which are surrounded by steel remain low.

— Results under C: This calculation has been carried out to investigate whether imperfections in the bonding between rubber and steel will lead to failure of the suspension ring. To simulate a defect, a few supported nodes on the boundary between the points F and S have been released. The results of the calculation are shown in Figure 5.6. Comparing the results with those for a perfect bonding, it is observed that the geometry is very sensitive even for small flaws in the bonding. The peak stresses in the critical area near point S are increased, and it is unlikely that a process in which the rubber is ripped off the steel will be arrested.

The numerical values of the displacements and the stresses near points D and E and the maximum stress near the rubber-steel interface are summarised in Tables 5.3 and 5.4. Because of the sensitivity of the original design for imperfections in the rubber-steel bonding, this design must be rejected. A decrease of the high stresses near points S and F can probably be achieved by enlarging the skirt in the triangle DFS. The second geometry is adapted in this direction.

5.3.2 Model 2

For the second model (Figure 5.7), the following calculations have been carried out:
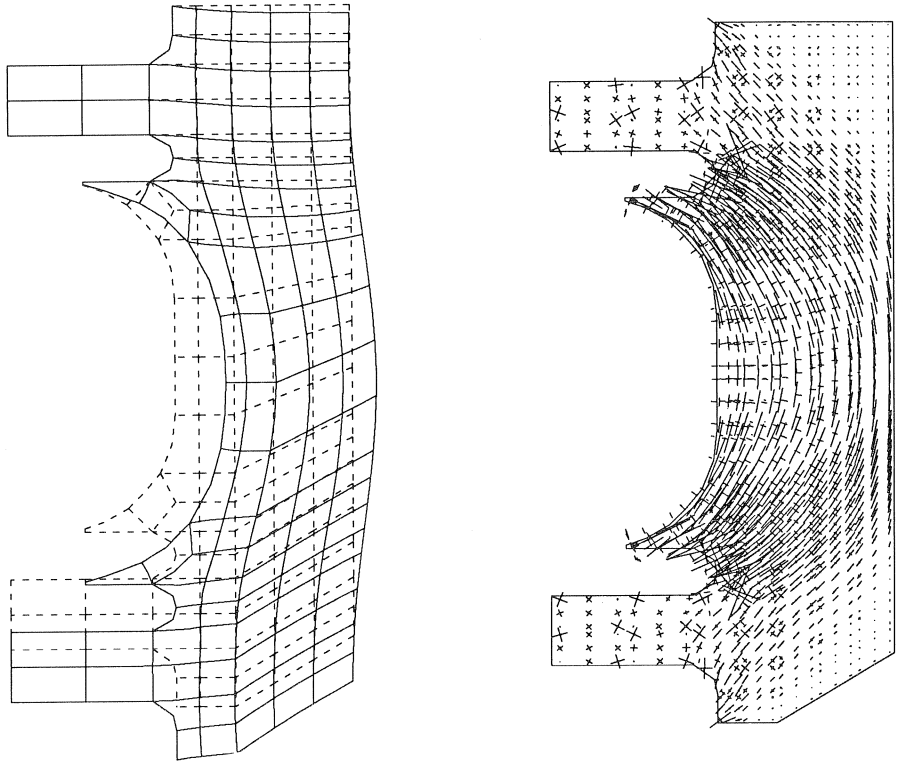
33
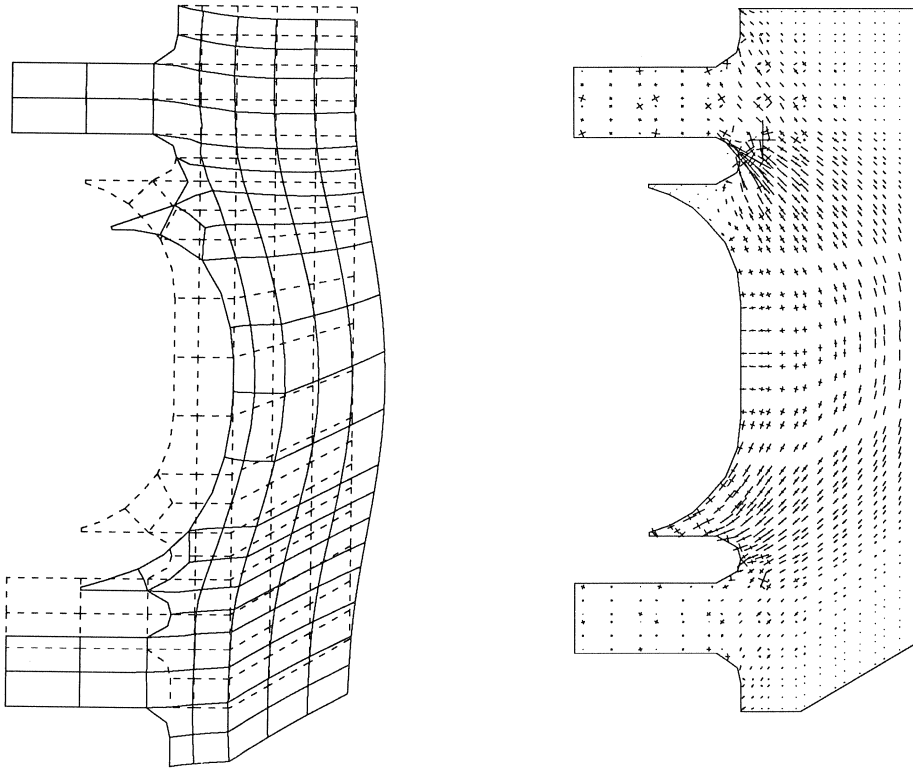
Fig. 5.5. Deformed and undeformed element mesh (left), and Cauchy stresses (right) for geometry 1 at a load factor of 1.0. As in the subsequent pictures of deformed specimens the deformations have not been scaled (i.e., are not exaggerated).

A.   Calculation of the displacements and stresses due to an internal gas pressure of 5.6 bar at a surrounding temperature of 65°C .

B.   Calculation of displacements and stresses, under the same loading case as mentioned in A, due to separation of the rubber-steel interface.

— Results under A: Figure 5.7 shows, that the tensile stresses still reach a maximum on places where, due to manufacturing process, it is difficult to obtain a good bonding. It is recalled that, from a engineering point of view, it is highly desirable to have compressive or shear stresses in bonding areas rather than tensile stresses. Just as in the original design it appears that the elements which are surrounded by the steel are lightly stressed.

Fig. 5.6. Deformed and undeformed element mesh (left), and Cauchy stresses (right) for geometry 1 with imperfections at a load factor of 1.0.

— Results under B: This calculation has been carried out to analyse whether insufficient bonding on the end faces will lead to failure. The unsupported nodes which simulate the ripping-off of the rubber-steel interface are located near point C of Figure 5.3. The deformations are similar to those of the first geometry, but the stresses near the crack tips have not increased compared with the undamaged model. From Table 5.4 (maximum stress near the bonding surface) it appears that if de-bonding occurs, this will not cause failure of the rubber structure.

To sum up, it appears, that this geometry is less sensitive for partial failure of the rubber-steel bonding than the first design. Nevertheless, the rubber material attached to the cut in the steel of the visco-seal still remains lowly stressed. The next step in the design procedure is to omit these unused rubber parts. This results in the third geometry.
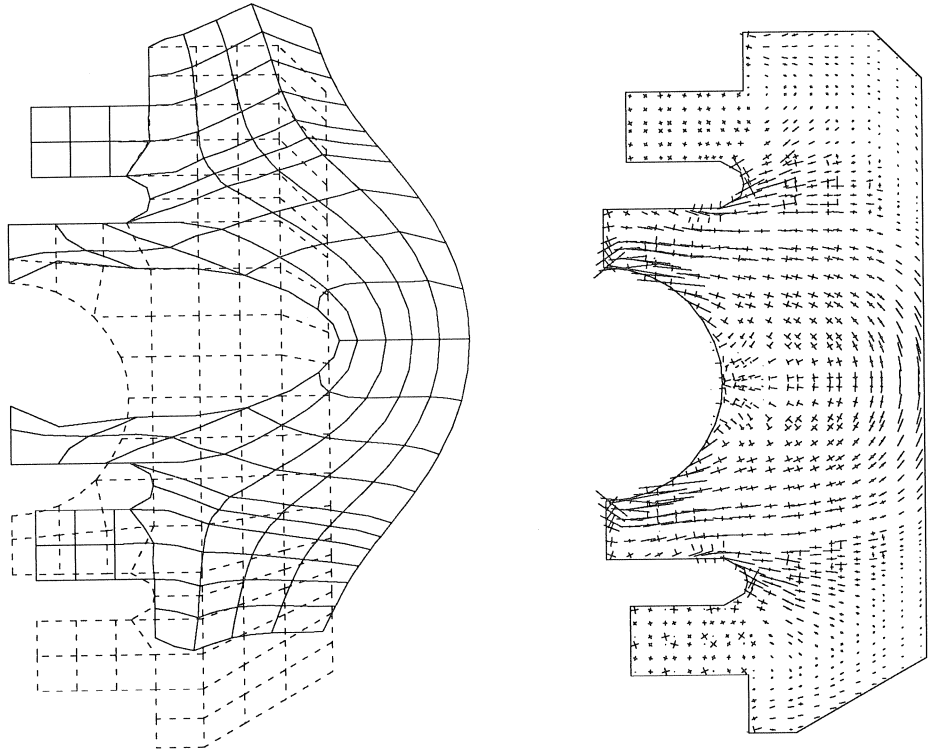
Fig. 5.7. Deformed and undeformed element mesh (left) and Cauchy
stresses (right) of geometry 2 at a load factor 5.0.

5.3.3 Model 3

For model 3 only a limited number of calculations have been carried out. The stress distribution due to internal gas pressure has been determined, but a failure analysis of the rubber-steel bonding has been omitted.

In Figures 5.8 and 5.9 the deformations and the stress distribution are given. This geometry gives a homogeneous stress distribution in the central part. Owing to the presence of compressive stresses at the end of the rubber-steel bonding, it is expected that a small imperfection of the bonding will not lead to a progressive failure of the suspension ring. Yet, there are still areas where the stresses remain low, and there is an area between the points F and G which shows high tensile stresses. As a result of the incompressibility of the rubber and the relative long skirts of the ring the radial displacement will increase. A further improvement of the design leads to the fourth geometry.
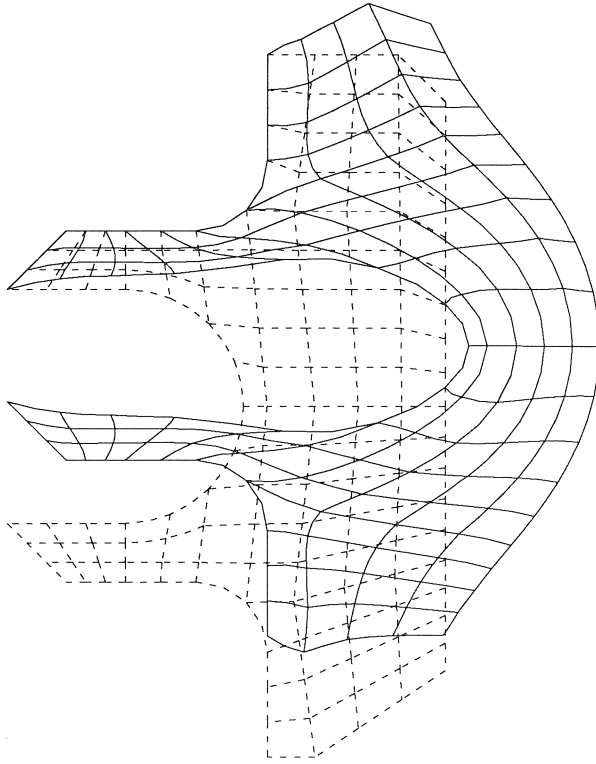
Fig. 5.8. Deformed and undeformed element mesh of geometry 3 at load factor 5.0.

5.3.4 Model 4

Figures 5.10 and 5.11 give the displacements and the stress distribution of geometry 4. In this model the low stressed areas have been 'cut-off' and replaced by steel. The advantage of this replacement is that the bonding area increases and that the radial displacements decrease. The numerical results of the calculation are again given in Tables 5.3 and 5.4.

So far, the calculations have been carried out for a conservative internal gas pressure. However, in reality the direction as well as the area of the surface on which the gas pressure acts will change. Since the gas pressure is constant the change in direction and area affects the total force that is exerted on the suspension ring. The effect of this phenomenon, known as non-conservative loading, has been investigated for this model. A quantitative comparison for the displacements and Cauchy stresses is summarised in Tables 5.5 and 5.6 for some significant points of model 4. It is observed that, for the
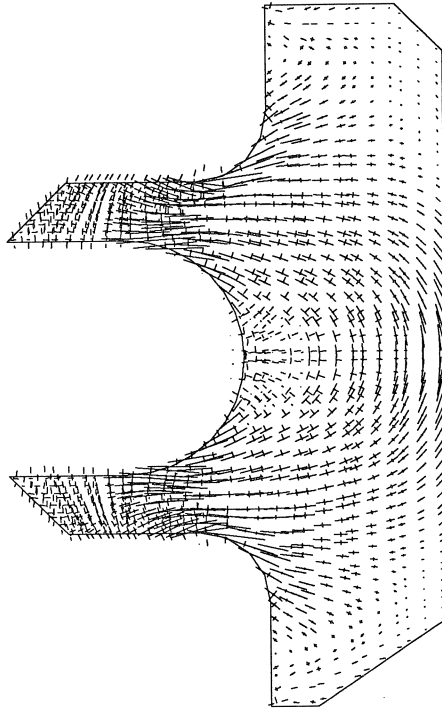
Fig. 5.9. Cauchy stresses for geometry 3 at load factor 5.0.

calculations with a non-conservative load, the radial displacements of the inner boundary increase and that the radial displacements of the outer boundary decrease compared with the results for conservative loading. As a result thereof, a more homogeneous stress distribution in the middle cross section is obtained. Because of the enlarged loading area the total resulting force will increase and a larger displacement can be expected compared with the calculation with a conservative loading. The increased stresses in the middle cross section can be explained in a similar way, since the equilibrium condition must be satisfied.

The deformations shown in Figure 5.10 and the Cauchy stresses shown in Figure 5.11 have been calculated for a non-conservative loading. It is observed from Figure 5.10 that the inner boundary CDF remains a proper circle, while in calculations with a conservative loading this boundary attains an ellipsoidal shape.
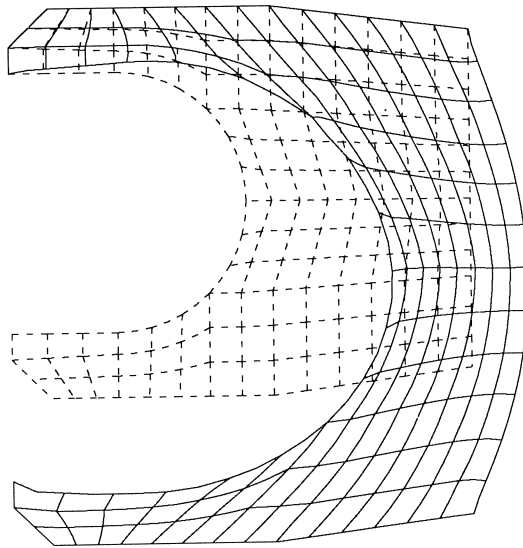
Fig. 5.10. Deformed and undeformed mesh of geometry 4 at a load factor 5.0.
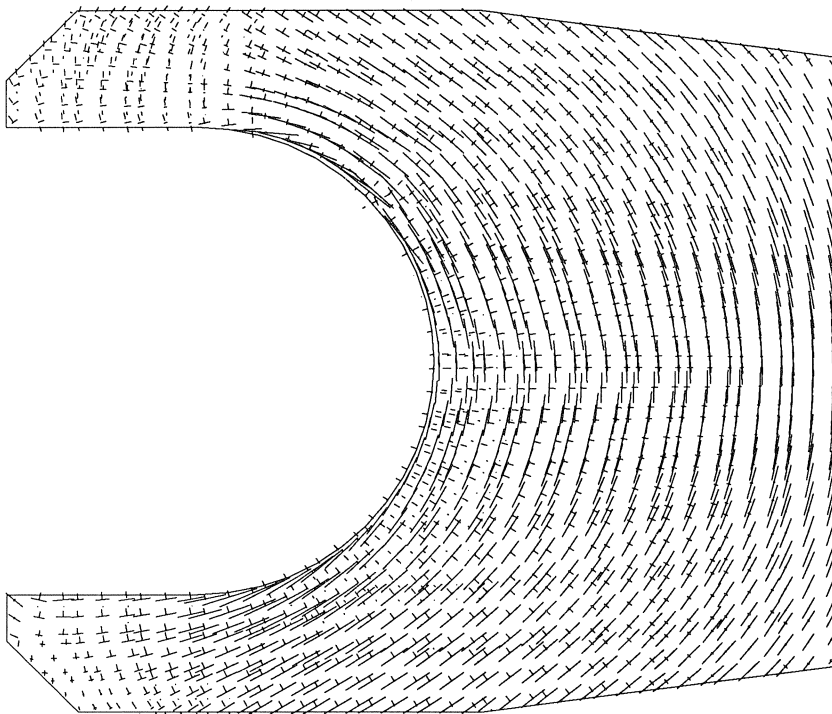
Fig. 5.11. Cauchy stresses for geometry 4 at a load factor 5.0.

39

Table 5.3. Radial Displacements u_r of the suspension ring in mm: load factor = 1.0.

PLACE	plane strain 2*2	axisymmetry 2*2	axisymmetry 3*3
MODEL 1			
point D	2.86	--	2.16
point E	2.04	--	0.98
imperfect bonding:			
point D	3.43	--	2.52
point E	2.52	--	1.33
MODEL 2			
point D	1.85	1.75	1.75
point E	1.25	1.17	1.14
imperfect bonding:			
point D	2.01	--	--
point E	1.37	--	--
MODEL 3			
point D	2.08	--	1.96
point E	1.42	--	1.31
MODEL 4			
point D	1.41	1.32	1.32
point E	0.66	0.61	0.61
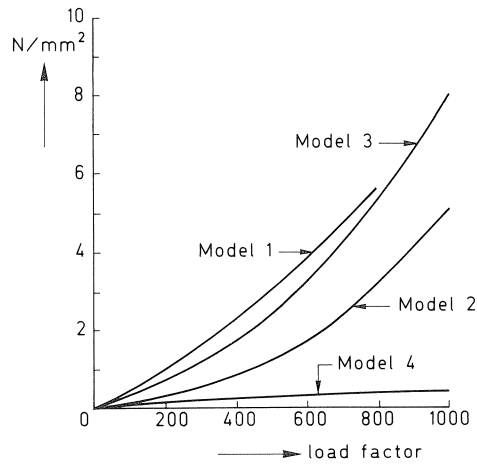
Fig. 5.12. Evolution of greatest Cauchy stress near steel border for each design.

Table 5.4. Axial Stresses σ_{zz} in the suspension ring in N/mm^2: load factor = 1.0.

PLACE	plane strain 2*2	axisymmetry 2*2	axisymmetry 3*3
MODEL 1			
point D	-0.41	--	0.013
point E	0.53	--	0.83
max. stress on the bonding surface	1.51	--	1.67
imperfect bonding:			
max. stress on the bonding surface	3.05	--	3.05
MODEL 2			
point D	-0.33	-0.34	-0.38
point E	0.41	0.44	0.30
max. stress on the bonding surface	0.75	0.78	1.19
imperfect bonding:			
max. stress on the bonding surface	0.75	--	--
MODEL 3			
point D	-0.28	--	-0.18
point E	0.48	--	0.51
max. stress on the bonding surface	0.69	--	0.85
MODEL 4			
point D	0.06	0.092	0.064
point E	0.47	0.48	0.49
max. stress on the bonding surface	0.25	0.18	0.15

Table 5.5. Radial Displacements u_r for model 4 in mm: load factor = 1.0, axisymmetric stress situation, 3*3 integrated.

PLACE	conservative	non-conservative
point D	1.32	1.74
point E	0.61	0.35

Table 5.6. Axial Stresses σ_{zz} for model 4 in N/mm^2: load factor = 1.0, axisymmetric stress situation, 3*3 integrated.

PLACE	conservative	non-conservative
point D	0.064	0.65
point E	0.49	0.85
max. stress on the bonding surface	0.15	--

5.3.5 Concluding remarks

Originally, the models have been analysed with plane strain elements. A comparison (Tables 5.3 and 5.4) shows that the analyses for an axisymmetric stress situation result in a stiffer response. This is because of the introduction of the tangential stress band in the axisymmetric models. The radial displacements in the middle cross section are smaller, while the stresses are mostly larger. However, the differences between the results of the calculations with axisymmetric and those with plane strain elements are less important than the choice of the strain energy function and the selection of the appropriate material parameters.

The models 1, 2, 3 and 4 have been produced and tested for a lifetime evaluation in a pilot plant. The test results revealed only marginal differences from the calculations. According to the calculations, the fourth design showed the best behaviour. The obtained homogeneous stress distribution provides a solid basis for a sound design and an extended life compared with the previous designs. This is shown in Fig. 5.12, which gives the highest tensile stresses near the rubber-steel interface of the four models. It is mentioned that the shear stresses in the fourth model exceed the normal stresses, but, as stated before, the rubber-steel interface is able to sustain much higher shear stresses than normal stresses.

6. Shock cell

The example discussed in this chapter is a shock cell which is loaded primarily in shear. Numerical experiments have been carried out without and with predefined cracks in order to investigate whether crack initiation would lead to progressive failure. The numerical results are furthermore compared with experiments and with a grossly simplified hand calculation.

6.1 Introduction

In civil engineering shock cells are used as a part of heavily loaded structures like fenders near sluices or in mooring structures. An example is the application of shock cells in the lockgates of the Eastern Scheldt Storm Surge barrier, which are loaded by wave attacks that are not necessarily perpendicular to the barrier. This results in an indirect displacement of the lockgates. Shock cells have been used to prevent damage accumulation between the steel lockgates and the concrete structure. In Figure 6.1 the function and the position of the shock cell in the structure is shown.

The shock cells have been manufactured by Royal Bakker Ridderkerk BV and consist of two enclosing steel cylinders of different diameters. The cylinders, which can move with respect to each other along the axis of symmetry, are connected by a rubber structure according to the sketch of Figure 6.2. The inner cylinder is supported by the barrier,
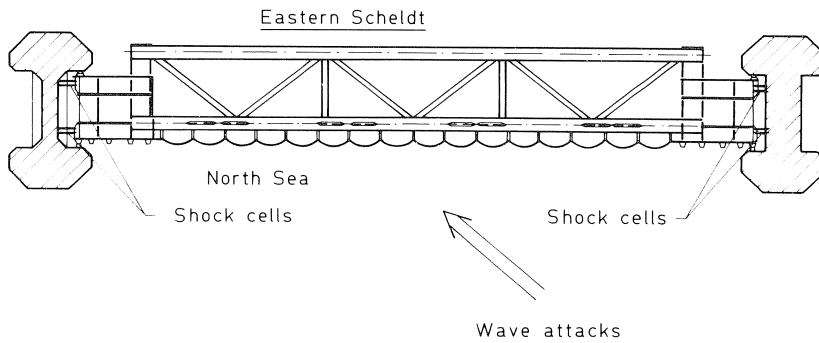
42

Fig. 6.1. Place and function of the shock cell in the Eastern Storm Surge barrier.
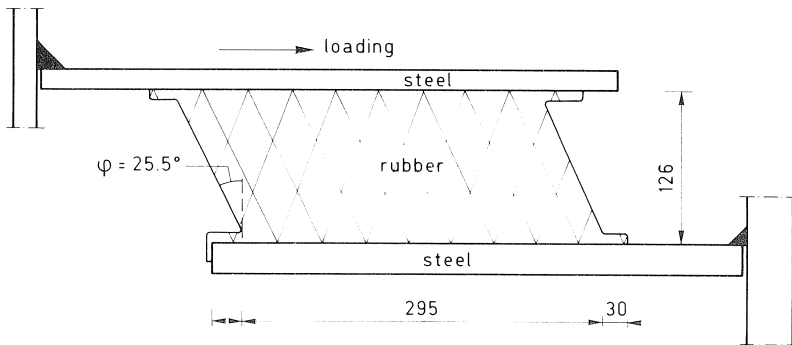

Fig. 6.2. Geometry and loading of the shock cell.

while the outer cylinder is loaded by the wave attacks on the gates. This load case can be modelled by applying a force or a prescribed displacement on the outer cylinder parallel to the axis of symmetry. Because displacement control usually results in a faster convergence, the latter possibility has been chosen.

6.2 Calibration of the numerical model

In the calculations for the shock cell the incompressible Mooney-Rivlin material model has been used. The material parameters have been determined independently at the TNO Plastics and Rubber Research Institute (KRI-TNO) and at Rijkswaterstaat (RWS). The parameter determination at Rijkswaterstaat was based upon experimental data of the manufacturer of the shock cells, while the TNO Plastics and Rubber Research Institute has carried out independent elongation tests. Table 6.1 lists the values of the parameters K_1 and K_2 for a virgin as well as for a pre-stressed material for both measurements. A difference is observed between both parameter identifications, but for the type of

Table 6.1. Material parameters for the Mooney-Rivlin model.

Determined by	$K_{1,virgin}$ [N/mm^2]	$K_{2,virgin}$ [N/mm^2]	$K_{1,pre}$ [N/mm^2]	$K_{2,pre}$ [N/mm^2]
RWS	0.334	0.475	----	----
KRI-TNO	0.258	0.618	0.317	0.296

deformation to which the shock cell is subjected (mainly shear) this discrepancy is not considered to be important. For pure shear only the sum of K_1 and K_2 is of interest as has been demonstrated in Chapter 2 (eq. (2.42)). When the values of $K_{1,virgin}$ and $K_{2,virgin}$ from Table 6.1 are added for the Rijkswaterstaat as well as for the KRI-TNO measurements, only a slight difference remains, namely 0.809 vs. 0.876 N/mm^2. So, the results of an analysis of the shock cell will be virtually the same for both sets of constants. In the final analysis the material constants as determined for a prestressed material have been used (Table 6.1).

To check the finite element model and the adopted Mooney-Rivlin constants, two simple tests calculations have been carried out for different geometries and have been compared with analytical solutions. First, the upper edge of a rectangle with a length $L = 295$ mm and a height $H = 126$ mm is displaced horizontally while the lower edge is supported. Secondly, a parallellogram with the same length and height and an internal angle of 22.5° is loaded in the same way. Both geometries and their prescribed deformation are shown in Figure 6.3.

According to the analytical solution of Chapter 2 the total force of a rubber specimen loaded in pure shear is given by:

$$F = 2 (K_1 + K_2) L \tan\phi \qquad (6.1)$$

with ϕ the angle of rotation of the sides of the rectangle and parallellogram, and L the length of the upper edge. The angle ϕ can be calculated from the horizontal displacement u of the upper edge according to $\tan\phi = u/H$. The maximum axial displacement that the outer cylinder of the shock cell can undergo, is $u = 104.71$ mm. Substition of this value in (6.1) gives for the Mooney-Rivlin constants of Rijkswaterstaat $F = 396.2$ N. The finite element calculation gives a total horizontal force of 396.8 N, which is within 0.2% of the hand calculation. For the second geometry a horizontal displacement $u = 104.71$ mm gives a angle of rotation $\phi = 31.7°$. The same approach now results in $F = 329.7$ N while the numerical analysis results in a total force $F_{comp} = 319.4$ N. For this geometry the difference between the analytical and computer calculation is thus 3.1%. These comparisons show that the differences between the finite element model and the hand calculation are small, at least with respect to the global
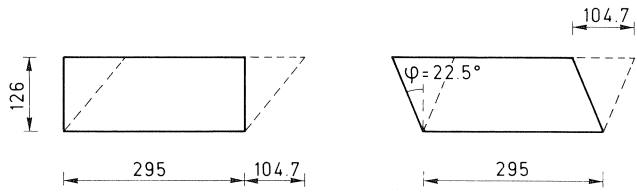
Fig. 6.3. Geometries for calibration of the finite element model.
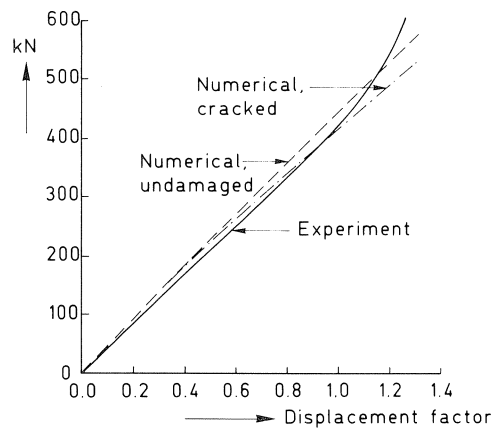

Fig. 6.4. Total force in axial direction for the undamaged shock cell.

behaviour of the structure. However, it is not possible to accurately predict the peak stresses by a hand calculation.

Apart from the computer simulation and the analytical solution, an experimental measurement of the stiffness of the shock cell has been made. In this experiment the axial force has been determined as a function of the imposed axial displacement. The resulting force-displacement relation is represented in Figure 6.4 by the solid line. The other two curves of Figure 6.4 represent numerical results respectively for an undamaged model and for a model with predefined cracks (Figures 6.5 and 6.8). The model with predefined cracks responds somewhat weaker than the undamaged model, but the difference is small. Both solutions are in close agreement with the experiment.
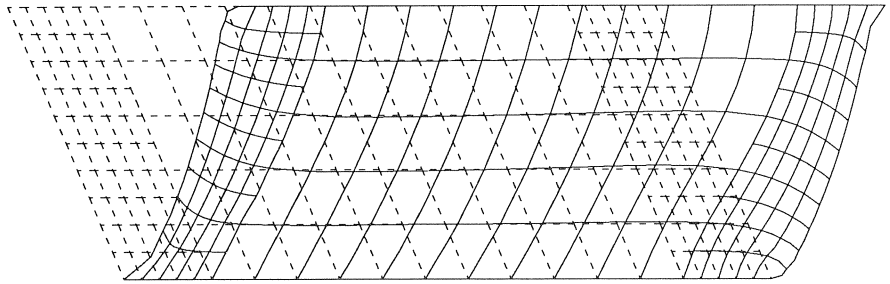
Fig. 6.5. Deformed and undeformed element mesh at ultimate load.
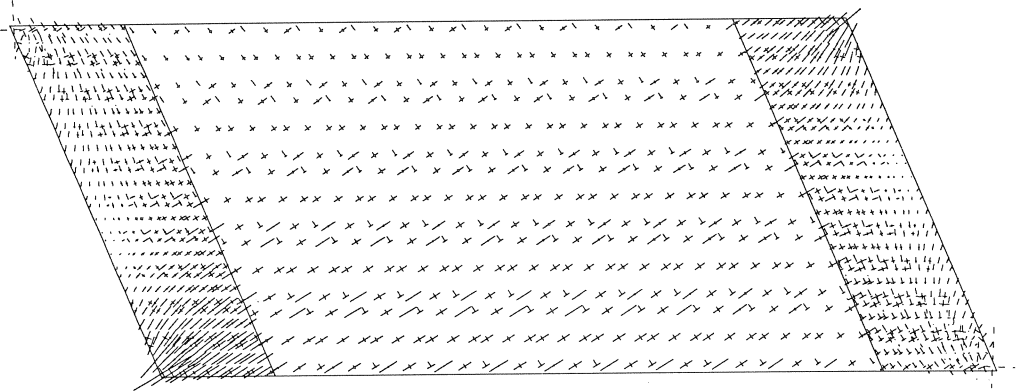
Fig. 6.6. Cauchy stresses at ultimate load.

6.3 Results

6.3.1 Undamaged shock cell

In the preceding section the correlation between numerical and experimental results of the global behaviour of the shock cell turned out to be rather good, which gives confidence in the calculated stresses. Figure 6.5 shows the original element mesh (the dotted lines) and the deformed model at ultimate load, which is defined as the loading when the maximum displacement of the outer cylinder is reached. The stress distribution at the same load is given in Figure 6.6. This stress distribution reveals that the largest stresses occur in the corners of the structure.

When we scrutinise the principal stresses in the Gauss points of one element more closely, a slight checker-board pattern in the stress distribution is observed. The stresses near the corners of an element, which is integrated with a 3*3 scheme, deviate from the
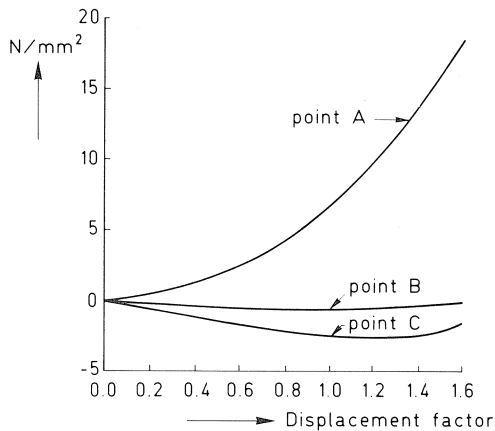
Fig. 6.7. Load versus Cauchy stress in some critical points.

other stresses which are all in the same range. The high peak stresses in the corners of the shock cell can be attributed to this checker-board stress distribution, and, therefore, do not have significance for the interpretation of the mechanical behaviour of the shock cell. An improved stress distribution can be obtained if a linear instead of of a bilinear interpolation of the (discontinuous) pressure field is used [7,16].

In Figure 6.7 the greatest principal Cauchy stresses points have been plotted as a function of the displacement factor of the outside cylinder for the following points: the intersection of the left boundary and the bottom (henceforth denoted as point A), the middle of left boundary (point B) and the intersection of the left boundary and the top (point C). The tensile stress near point A amounts 6.5 N/mm^2 for a displacement factor of 1.0 and increases even up to 18 N/mm^2 for a displacement factor of 1.6, while the allowable tensile stress of this rubber compound is about 2 N/mm^2. Tearing of the rubber in the corners of the shock cell is therefore very likely. A next step in the analysis is to simulate the internal tearing process of rubber by introducing some predefined cracks.

6.3.2 Shock cell with predefined cracks

The predefined cracks near the corners of the shock cell have been modelled in the same manner as in the preceding analysis of the suspension ring. At the boundary of the first and second row of elements in the mesh refinement near point A some nodes are added at same place as the original nodes. In this way the upper edge of the first row of elements can undergo an independent displacement relative to the lower edge of the second row of elements.
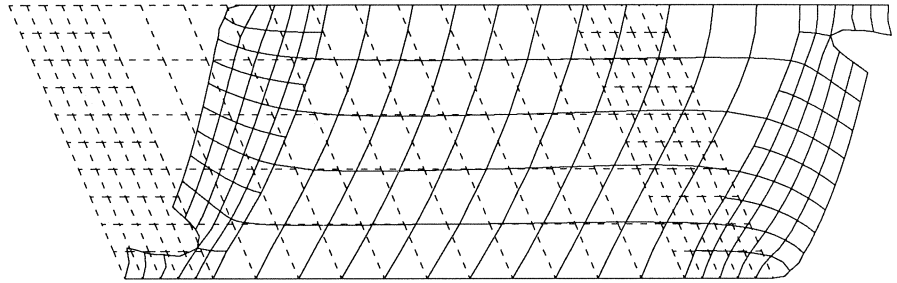
47

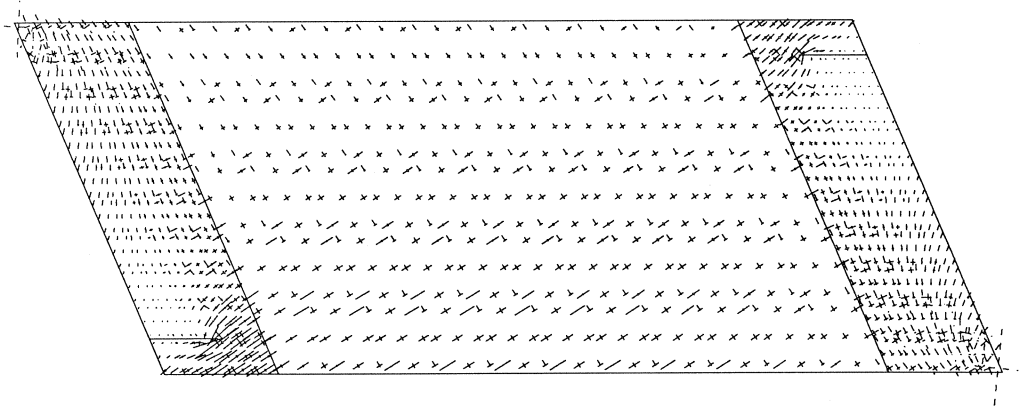Fig. 6.8. Deformed and undeformed element mesh at ultimate load.

Fig. 6.9. Cauchy stresses at ultimate load.

Figure 6.8, which gives a deformed and an undeformed element mesh, shows that the two cracks are wide open at a displacement factor of 1.0. Figure 6.9 gives the corresponding stress distribution. Figures 6.8 and 6.9 suggest a continued tearing process, which is confirmed by value of the major principal stress near the crack tip (point D): 4.8 N/mm^2. The evolution of the Cauchy stress is summarised in Figure 6.10 for points A, B, C and D.

In summary, we can conclude that there is a close agreement between the numerical, analytical and experimental results with regard to the overall behaviour of the shock cell. A finite element calculation is particularly useful for a prediction of the peak stresses that occur near the corners of the rubber specimen.
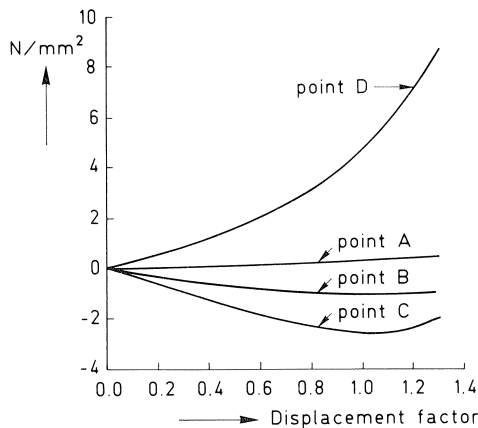
Fig. 6.10. Load versus Cauchy stress in some critical points.

7. Three-dimensional analysis of a supporting block

The two examples discussed in the preceding chapters are loaded mainly in tension (the suspension ring) and in shear (the shock cell). The numerical results for the suspension ring and for the shock cell only differ slightly from the experimental results. In this section the attention will be confined to the simulation of the structural behaviour of a rubber specimen that is primarily loaded in compression. The example discussed in this section is a supporting block for bridges and other heavily loaded structures. The Mooney-Rivlin strain energy function extended for compressibility has been employed to calculate the stresses and deformations. The deformations have been computed for various values of the bulk modulus and the material constants K_1 and K_2.

7.1 Description of the problem

The supporting block is a layered rubber-steel package of 200*100 mm and consists of two rubber layers of 33 mm thick, separated by a steel plate of 6 mm. The purpose of the calculation is to compare the calculated and measured forces and deformations, and to investigate whether or not a compressible form of the strain energy function results in a better numerical simulation of the mechanical behaviour of rubberlike materials in compression. The comparison between the calculated and the measured values is carried out for a uniform compression, which is obtained by prescribing a uniform vertical displacement of the upper steel plate.
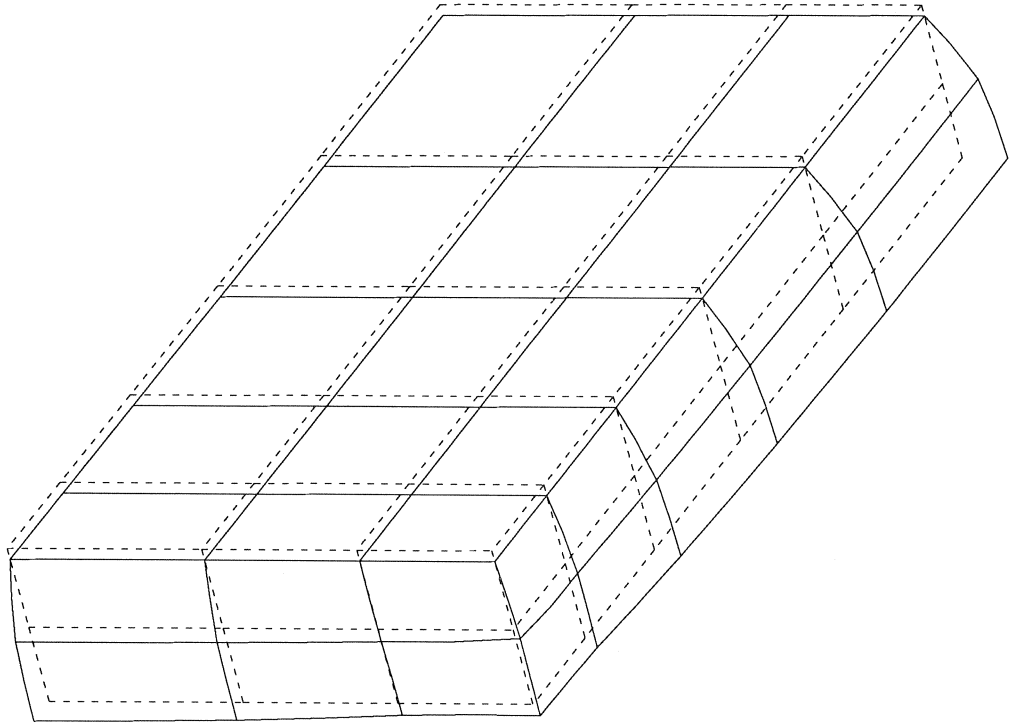
49

Fig. 7.1. Deformed and undeformed element mesh of the supporting block
at a vertical displacement of 7% of the height.

The example is quite interesting, since apart from problems that relate to the constitutive relation for rubberlike materials, difficulties were encountered in obtaining a properly converged solution. It appears that relatively fast converging solutions can be obtained for extensions up to several hundreds of percents, while convergence is hard to achieve only after a few percent compression.

7.1.1 Calculations and measurements of the supporting block

The finite element model and the state of deformation under compression is given in Figure 7.1. By virtue of three-fold symmetry only one-eighth of the geometry has been modelled. Because of the expected large strains near the free edges of the block the element mesh has been refined at that place (Figure 7.1). For the finite element modelling a twenty-noded three-dimensional element with one internal pressure node has been used,
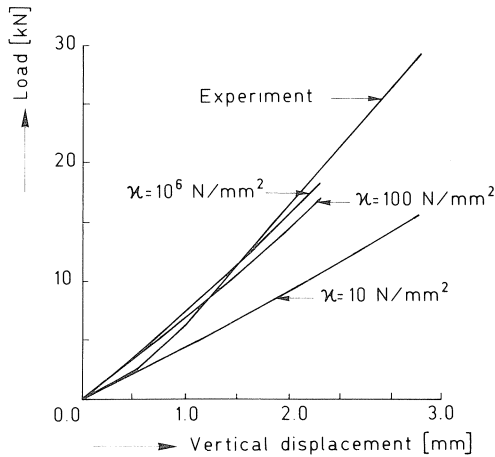
Fig. 7.2. The total force as a function of the vertical displacement
for various values of the bulk modulus κ.

which results in a total of sixty-one degrees-of-freedom. The steel plate at the upper side of the block has been modelled with eight-noded plane stress elements.

The load-deflection curves from the measurements and from the calculations, which have been carried out for a logarithmic range of values of the bulk modulus κ, are given in Figure 7.2. The results in this figure have been obtained with $K_1 = 0.16$ N/mm^2 and $K_2 = 0.49$ N/mm^2 as constants of the Mooney-Rivlin strain energy function. When the the bulk modulus is chosen in the same order as the Mooney-Rivlin constants, say $\kappa = 10$ N/mm^2, a rather soft response is obtained. For high values of the bulk modulus κ the contribution of deviatoric stiffness, which can be related to the sum $K_1 + K_2$, becomes less important. The load-deflection diagram for $\kappa = 1000$ N/mm^2 is almost the same as the diagram for $\kappa = 10^6$ N/mm^2. In Figure 7.3 the influence has been plotted of a variation of the sum $K_1 + K_2$, while the bulk modulus has been kept constant at $\kappa = 1000$ N/mm^2. When the sum is increased from 0.65 N/mm^2 to 0.75 N/mm^2 the supporting block reacts significantly stiffer. It is mentioned that with a compressibility $\kappa = 100$ N/mm^2 a similar shift of the load-deflection curve has been found.

In addition to the force-displacement relation, the horizontal displacement of the midpoint on the longest side of the rubber block has been recorded. The results of the measurement and the calculations are presented in Figure 7.4. Again, no difference is found when κ is increased from 1000 to 10^6 N/mm^2.

Because of the large deviation between the measured and calculated horizontal displacement, a global volume check has been made for one quarter of the block with a bulk modulus $\kappa = 1000$ N/mm^2. For the volume check the upper plate is moved downwards
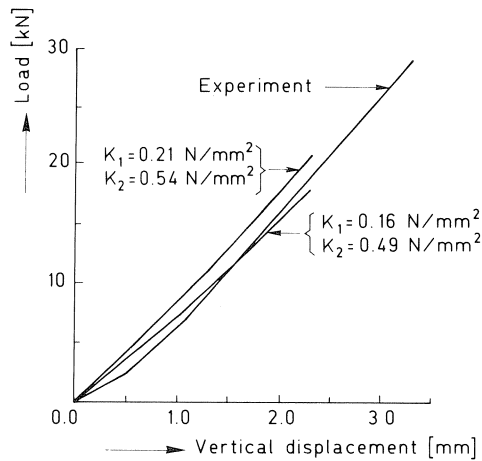
Fig. 7.3. The total force as a function of the vertical displacement
for different sums of the material constants K_1 and K_2.

over 2 mm. The calculated horizontal deformations have approximately a quadratic shape over the height and the displacements along the two sides are assumed to vary linearly. The original volume of the block is 165,000 mm^3 and the displaced amount of rubber at the top is 2*100*50 = 10,000 mm^3. The estimated displaced amount of rubber along the short side is 2,400 mm^3 and 5,600 mm^3 along the long side. This approximation results in a volume decrease of about 2,000 mm^3 or 1.2%.

On the other hand an analytical estimation can be made for the volume decrease when a vertical displacement of 2 mm of the steel plate is enforced. According to Figure 7.2 the force at 2 mm vertical displacement is about 4 kN for a quarter of the block. This results in a hydrostatic pressure of about 0.8 N/mm^2. According to equation (2.29) this pressure level requires a bulk modulus that is smaller than κ = 100 N / mm^2 so as to obtain a volume decrease of about 2,000 mm^3. This is consistent with the outcome of the numerical analyses.

The horizontal displacements that have been recorded in the measurements therefore suggest an extremely compressible material behaviour. To obtain a better approximation of the lateral displacement a very low value for the bulk modulus and very high values for K_1 and K_2 must be used in a numerical analysis. Nonetheless, such values for κ, K_1 and K_2 are unrealistic. At the present stage it can only be concluded that experimental evidence suggests that the compressibility of rubber can not be neglected as is often done, but that the extreme compressibility recorded in the experiment can not be explained from calculations in which accepted values for the bulk modulus have been substituted.
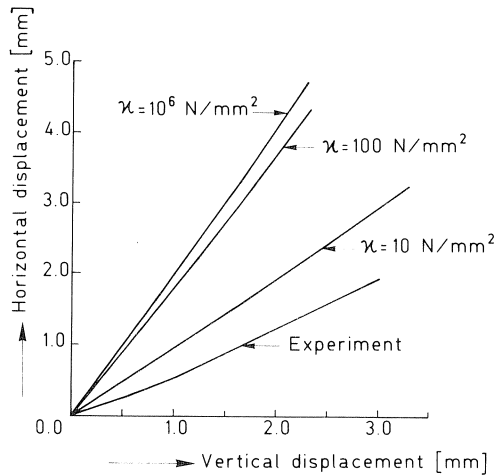
52

Fig. 7.4. The horizontal displacement versus the lateral displacement
for a different sum of the bulk modulus κ.

8. Concluding remarks

In this article a rather comprehensive account has been given of the possibilities of finite elements to predict deformations and stresses in rubber structures. Constitutive models for rubber, the governing finite element equations, the parameter determination, and a number of applications have been discussed.

Contrary to most studies that have been reported in the literature, the compressibility of rubber is not necessarily neglected. Experimental evidence contradicts such a hypothesis as has for instance been shown in one of the examples. The present formulation employs a separate interpolation of the displacement and the pressure field to reduce the danger of 'locking' of finite elements in (nearly) incompressible media. A strictly incompressible solid is easily obtained within this formulation simply by setting the compressibility equal to zero.

The numerical results of the examples have been compared with experiments. In general, the agreement appeared to be rather good. Yet, it would be incorrect to suggest that the discussed techniques can be used easily and in a routine-like manner. Calculations as described herein require skill and knowledge to be carried out successfully. The advantage of numerical tools is that, once the computer code is available, a number of variants can be analysed quickly and understanding is built up how the design can be altered such that for instance undesirable peak stresses are avoided.

With the models described in this article a large variety of rubber problems can be solved numerically. However, it is definitely not suggested that accurate predictions of

53

deformations and stresses can be made for *all* problems involving rubberlike material behaviour. To broaden the class of problems which can be solved reliably, more research has to be done with respect to the numerical treatment of rubber components in the compressive regime since we then face the problem of bifurcations and lack of stability. Also, additional numerical tools must be implemented to model contact problems, tearing of rubber specimens, and reinforcement in rubber structures.

References

[1] Oden, J.T., Finite elements of nonlinear continua. McGraw-Hill, New York (1972).

[2] Hill, R., On uniqueness and stability in the theory of finite elastic strain. J. Mech. Phys. Solids, Vol. 5, pp. 229-241 (1957).

[3] Rivlin, R.S, Stability of pure homogeneous deformations of an elastic cube under dead loading. Q. Appl. Math., pp. 265-271 (1974).

[4] Becker, E. and Bürger, W., Kontinuumsmechanik. Teubner, Stuttgart (1975).

[5] Penn, R.W., Volume changes accompanying the extension of rubber. Trans. Soc. Rheology, Vol. 14, pp. 509-517 (1970).

[6] Peng, S.T.J. and Landel, R.F., Stored energy function and compressibility of compressible rubberlike materials under large strain. J. Appl. Physics, Vol. 46, pp. 2599-2604 (1975).

[7] Sussman, T. and Bathe, K.-J., A finite element formulation for nonlinear incompressible elastic and inelastic analysis. Computers and Structures, Vol. 26, pp. 357-409 (1987).

[8] Ogden, R.W., Large deformation isotropic elasticity - On the correlation of theory and experiment for compressible rubber-like solids. Proc. Roy. Soc. London, Vol. A328, pp. 567-583 (1972).

[9] Jankovich, E., Leblanc, F., Durand, M. and Bercovier, M., A finite element method for the analysis of rubber parts, experimental and numerical assessment. Computers and Structures, Vol. 14, pp. 385-391 (1981).

[10] Häggblad, B. and Sundberg, J.A., Large strain solutions of rubber components. Computers and Structures, Vol. 17, pp. 835-843 (1983).

[11] Scharnhorst, T. and Pian, T.H.H., Finite element analysis of rubber-like materials by a mixed model. Int. J. Num. Meth. Eng., Vol. 12, pp. 665-676 (1978).

[12] Glowinski, R. and Le Tallec, P., Finite elements in nonlinear incompressible elasticity. In: Finite Elements: Special Problems in Solid Mechanics (Eds. J.T. Oden and G.F. Carey), Ch. 2, pp. 67-93 (1985).

[13] Mooney, M., A theory of large elastic deformations. Journal of Applied Mechanics, Vol. 11, pp. 582-592 (1940).

[14] Rivlin, R.S., Large elastic deformations of isotropic materials IV. Further developments of the general theory. Phil. Trans. Roy. Soc., Vol. A241, pp. 379-397 (1948).

[15] Zienkiewicz, O.C., The Finite Element Method. McGraw-Hill, New York (1977).

[16] Hughes, T.J.R., The Finite Element Method. Linear Static and Dynamic Analysis. Prentice-Hall, New Jersey (1987).

[17] Crisfield, M.A., Finite Elements and Solution Procedures for Structural Analysis. Volume 1: Linear Analysis. Pineridge Press, Swansea (1987).

[18] Bathe, K.-J., Finite Element Procedures in Engineering Analysis. Prentice-Hall, New Jersey (1982).

[19] Bathe, K.-J., Ramm, E. and Wilson, E.L., Finite element formulations for large deformation dynamic analysis. Int. J. Num. Meth. Eng., Vol. 9, pp. 353-386 (1975).

[20] Fortin, M. and Fortin, A., Newer and newer elements for incompressible flow. In: Finite Elements in Fluids - Volume 6 (Eds. R.H.Gallagher, G.F. Carey, J.T. Oden and O.C. Zienkiewicz), Ch. 7, pp. 171-187 (1985).

[21] Soos, I., Assessment of rubber filler interactions from stress-strain curves (translated from Russian). International Polymer, Science and Technology, Vol. 12, pp. T34-T36 (1985).

[22] de Borst, R. and Blaauwendraad, J., Stability and spurious kinematic modes in strain-softening concrete. In: Proc. Int. Conf. on Computational Engineering Science, Springer Verlag, Berlin, in press (1988).

[23]   Rots, J.G. and de Borst, R., Analysis of mixed-mode fracture in concrete. ASCE Journal of Engineering Mechanics, Vol. 113, pp. 1739-1758 (1987).

[24]   Nagtegaal, J., Parks, D.M. and Rice, J.R., On numerically accurate finite elements in the fully plastic range. Comp. Meth. Appl. Mech. Eng., Vol. 14, pp. 153-177 (1974).

[25]   Treloar, L.R.G., The Physics of Rubber Elasticity. Clarendon Press, Oxford (1975).

Appendix: elaboration of incremental equations for 3D-analysis

Writing the derivatives $\dfrac{\partial I_1}{\partial \mathbf{C}}$, $\dfrac{\partial I_2}{\partial \mathbf{C}}$ and $\dfrac{\partial I_3}{\partial \mathbf{C}}$ as vectors, we obtain

$$\frac{\partial I_1}{\partial \mathbf{C}} = \begin{Bmatrix} 1 \\ 1 \\ 1 \\ 0 \\ 0 \\ 0 \end{Bmatrix} \tag{A.1}$$

$$\frac{\partial I_2}{\partial \mathbf{C}} = \begin{Bmatrix} C_{22}+C_{33} \\ C_{33}+C_{11} \\ C_{11}+C_{22} \\ -C_{21} \\ -C_{32} \\ -C_{13} \end{Bmatrix} \tag{A.2}$$

$$\frac{\partial I_3}{\partial \mathbf{C}} = \begin{Bmatrix} C_{22}C_{33} - C_{23}C_{32} \\ C_{33}C_{11} - C_{31}C_{31} \\ C_{11}C_{22} - C_{12}C_{21} \\ C_{23}C_{31} - C_{21}C_{33} \\ C_{31}C_{12} - C_{32}C_{11} \\ C_{12}C_{31} - C_{13}C_{22} \end{Bmatrix} \qquad\qquad (A.3)$$